HEAT TRANSFER ENHANCEMENT PHENOMENA AND PRESSURE DROP CHARACTERISTICS IN TWO-PHASE PULSATING FLOW USING R-134A

BY

YUHENG ZHANG

THESIS

Submitted in partial fulfillment of the requirements
for the degree of Master of Science in Mechanical Engineering
in the Graduate College of the
University of Illinois at Urbana-Champaign, 2017

Urbana, Illinois

Adviser:
Professor Xiaofei Wang

Abstract

The heat transfer and pressure drop aspect of a saturated two-phase flow imposed to periodic inlet mass flow rate were studied using both experimental and modeling approaches. The two-phase flow of R-134 was tested in a single pass, horizontal smooth copper tube coil with a 6.2 mm (0.244-in.) inner diameter. The test section uses aluminum plain fins 0.30 m (11.8-in.) long, 0.03 m (1.18-in.) wide and 0.3 mm (0.012-in.) thick. Heat was applied to the test section using external air flow at ambient temperature. The test parameters varied as follows: mass flux, 75 – 250 kg/m^2-s (55 – 184 klb$_m$/ft^2-hr); heat flux, 2-12 kW/m^2 (600-3800 Btu/hr-ft^2); vapor quality, 10-98 percent; saturation temperature 15 ^{o}C (59 ^{o}F); flow pulsation period (2-24 sec). The temporal pressure drop data was recorded and used as the basis of a newly proposed close-form model for predicting the heat transfer and pressure drop for pulsating two-phase flow based on the quasi-steady state assumption.

The enhancement of heat transfer in saturated boiling pulsating two-phase flow was found to be higher in shorter pulsation periods. It was also found that for low inlet vapor qualities and short pulsation periods, reduction in the pressure drop and enhancement in heat transfer coefficient could be achieved at the same time, which can be potentially beneficial to the system COP. Furthermore, the flow regime, which is a widely recognized factor having dominant influence on the heat transfer of two-phase flow, was also captured and analyzed in this study using high speed camera. Synchronized flow regime images and pressure drop data were also presented to demonstrate the relation between flow regime evolution and pressure drop variation with time as a potential means to identify the flow regime using the pressure drop characteristics.

Dedication

To my parents – Thank you!

Acknowledgments

The support by Professor Xiaofei Wang and the Air Conditioning and Refrigeration Center of the University of Illinois at Urbana-Champaign is gratefully acknowledged by the author.

Table of Contents

1 Introduction

1.1 Background

Pulsating flow, sometime also referred as pulsating, pulsed or pulsitle flow, characterized as peridic variation of one or some flow parameters, exists in numerous systems, such as arterial circulation, combustion engine, reciprocating compressor system and so on. It could be a natural response to the system operation, which is the case for most situations. Such as, some AC&R systems with a variable speed compressor [1-3]; pulse-driven cooling loops for spacecraft [4-6]; supercritical helium refrigeration loop for Tokamak type fusion reactors [7-9]; systems operating on off-shore platforms [10], etc. It also may be generated due to the flow instability. For example, the flow pulsation could be encountered in evaporators at the liquid and vapor two-phase region where the density fluctuation or pressure-drop oscillation are natural characteristics of the flow. Such fluctuations could generate misleading signals to the control module and result in the well-known "hunting" phenomena in AC& R systems [11-15]. Such flow pulsation/oscillation is also very common in microchannel heat exchanger and results in fluids maldistribution [16-18]. As the relevant engineering applications become increasingly prominent, it is very important to understand the flow dynamics and thermal behavior of pulsating flow for system performance improvement and control strategy development.

1.2 Literature review

The effect of flow pulsation on the heat transfer coefficient and pressure drop has been constantly investigated in the past few decades. Due to different heating methods, working fluids and pulsating mechanism conclusion drew from different works may vary. In the following sections, we organize the literatures by the topic of heat transfer performance and pressure drop. Both experimental and modelling work in this area is reviewed.

1.2.1 Heat Transfer in Pulsating Flow

Modeling Work

The effect of flow pulsation to the heat transfer from fluid to solid surface has been constantly investigated by experimental and analytical methods since the 1950s. Among the earliest works, Womersly [19] and Uchida [20] successfully obtained analytical velocity field solutions for single phase laminar flow in tubes driven by a pulsating pressure gradient. Later, Siegel and Perlmutter [21] obtained an analytical solution for the heat transfer problem from a single phase laminar flow subjected to a pulsating pressure gradient to a pair of parallel plates it flows within. They utilized the quasi-steady state assumption to calculate the instantaneous heat transfer coefficient from the flow to the plates during this transient heat transfer situation.

For single phase turbulent flow, the analytical model reaches its limit. In the turbulent regime, the quasi-steady assumption and empirical correlations were combined to predict the heat transfer in pulsating flow. Baird et. al [22] have shown how to express the ratio of the fluid side heat transfer coefficient between a pulsating flow and steady flow in a simplified form in terms of the characteristics of the velocity fluctuation. Baird's equation was based upon the following assumptions:

(a) Quasi-steady state concept, i.e. an assumption that the heat transfer coefficient at any instant can be predicted from the flow parameters at that instant using the steady flow correlations.

(b) The velocity fluctuation was a sinusoidal wave.

(c) The heat transfer coefficient is proportional to the nth power of the velocity.

Baird's equation for the ratio between pulsating flow heat transfer and steady flow heat transfer was a function of the following variables:

(d) Pulse frequency denoted by f in Hz

(e) Pulse Amplitude denoted by A in ft

(f) Mean velocity V_s in ft/sec

(g) Dimensionless pulsation velocity: $Y = 2\pi f \cdot A/V_s$

The equation for the ratio of heat transfer derived was written as follows:

$$R = \frac{h_{\text{pulsating}}}{h_{\text{steady}}} = \frac{\int_0^{2\pi} \left(\frac{V}{2\pi}\right)^n d\theta}{\left(\int_0^{2\pi} \frac{V}{2\pi} d\theta\right)^n} \tag{1}$$

where $h_{\text{pulsating}}$ and h_{steady} are the fluid side heat transfer coefficient of pulsating flow and steady flow respectively; n is an experimental constant. The instantaneous velocity V was assumed to be a sinusoidal function of time:

$$V = V_s + \frac{d}{dt}(A \cdot sin(2\pi ft)) = V_s(1 + Ycos(2\pi ft)) \tag{2}$$

Substituting equation (2) into equation (1):

$$R = \frac{1}{2\pi}\int_0^{2\pi} (1 + Ycos\theta)^n d\theta \tag{3}$$

Although analytical expression of equation (3) is not available, a numerical solution can be obtained. Baird et. al [22] simplified the velocity fluctuation to a square wave function and obtained an explicit expression of equation (3):

$$R = [(1 + 0.707Y)^n + |1 - 0.707Y|^n]/2 \tag{4}$$

It can be seen from equation (3) that the prediction of the pulsating-to-steady ratio of the fluid side heat transfer coefficient in a pulsating flow with a square wave velocity fluctuation always increases with the dimensionless parameter Y. As Y is proportional to the pulsation frequency and pulsation amplitude, and inversely proportional to the mean flow velocity, the equation further suggested that the ratio of heat transfer increases with the pulsation frequency and amplitude, but decreases with the mean velocity. Baird et. al [22] and later [23] reported data that showed excellent agreement with their theoretical equations.

It shall be expected from Baird's derivation that different velocity fluctuation profiles would cause distinct behaviors in the ratio of heat transfer. In the past several decades, many researchers have carried out experiments with different constructions that could produce distinct velocity fluctuations. Some of the studies are summarized in the next chapter.

The technique of flow pulsation can be realized in various configurations defined by the fluid type, the mean velocity, the pulsation frequency, the pulsation amplitude, and possibly some other factors. Many studies have been reported in the past on the effect of each factors described above.

Experimental Work - Effect of Fluid Type

Majority of past experimental investigations was carried out with water or air. Krishnan et. al [24] tested different fluids in a heat exchanger including air, water, glycol and engine oil for their heat transfer characteristics under the influence of flow pulsation from 0 to 7 Hz. They noted that the enhancement in heat transfer coefficient by flow pulsation was more pronounced with more viscous fluids. In their work, it was also noted that the enhancement in heat transfer coefficient was more pronounced in a shorter heat exchanger. Kim et. al [25] through numerical simulation; Elshafei et. al [26] and Habib [27] through experimental investigation reached a similar conclusion on the heat transfer enhancement variation with the tube length. They found that the enhancement in heat transfer coefficient was more noticeable in the entrance/thermally developing region of the flow passage. However, conflicting findings were reported by Karamercan et. al [28], who tested the heat transfer coefficient of water in a shell and tube heat exchanger. Their findings suggested that the augmentation in heat transfer coefficient increases as the length of the heat exchanger increases. With a tested range of frequency from 0 to 5 Hz, they observed as much as an 8-fold increase in the heat transfer coefficient.

Wang et. al [29] and Kærn et. al [30] investigated the effect of flow pulsation in two phase flow using R134-a. Both authors tested the heat transfer coefficient under similar range of frequencies and observed both enhancement and reduction in the heat transfer coefficient. Wang et. al found that the heat transfer coefficient increases monotonically with the pulsation frequency, where the highest frequency tested – 0.5 Hz produced as much as 127% enhancement in the heat transfer coefficient. Kærn et. al tested a range of frequency from 1 to 1/9 Hz. They found that the enhancement in heat transfer coefficient reached maximum value at a frequency of 0.125 Hz, which was much smaller than 0.5 Hz reported by Wang et. al. Kærn et. al also reported that the enhancement in heat transfer coefficient was more pronounced in tests with a larger heat flux.

There were also literatures where negligible effect from flow pulsation was reported. Hessami et. al [31] tested water in a single tube with a range of pulsation frequency from 0.1 – 1 Hz. They reported as much as 15% increase in the heat transfer coefficient. However, they claimed that this amount of enhancement was within the magnitude of experimental error, thus considered to be insignificant. Chen et. al [32] tested two phase R134-a in an annular duct, where they found the change in heat transfer coefficient negligible. However, it shall be noted that in Chen's paper only the results from a pulsation frequency of 1/120 Hz were reported, which was significantly lower than those tested by Wang and Kærn.

Experimental Work - Effect of Mean Velocity

In some literatures, the mean flow velocity of the baseline flow was reported to be an important factor for the enhancement in heat transfer coefficient. Baird et. al [22] tested water in a single tube test section with a wide range of Reynolds number. They found that the enhancement in heat transfer coefficient was greater for lower Reynolds number. The maximum amount of enhancement reported in their work was about 40%. Mackley et. al [33] also found that enhancement was more pronounced at low Reynolds number. Their tests also used water in a single tube, which produced as much as 30-fold increase in the heat transfer coefficient in low Reynolds number flow. Habib et. al [27] and Persoons et. al [34] carried out tests using water in a single tube and micro-channel heat sink, respectively. And they both reached the same conclusion that the enhancement in heat transfer coefficient increases with the decrease in the Reynolds number of the flow. Ludlow et. al [35] found that the enhancement does not always decrease as the Reynolds number increases. They reported that for water, the enhancement produced by flow pulsation was most pronounced in the laminar-turbulent transition region. Jacobi et. al [36] reported the same trend in air flow.

Experimental Work - Effect of Pulsation Frequency

Habib et. al [27] tested water in a curved tube and Rabadi et. al [37] tested water in a single tube with a frequency from 1 to 8 Hz. They both found that the heat transfer coefficient decreases with the pulsation frequency. Rabadi et. al [37] reported that the heat transfer coefficient decreases with pulsation amplitude at low pulsation frequency. On the other hand, Wang et. al [29] who tested two phase R-134a in a tube coil, Krishnan et. al [24] who tested various fluids, Baird et. al [23], Karamercan et. al [28], Ludlow et. al [35], Baird et. al [22] and Mackley et. al [33] who tested water in a single tube setup, all reported an increasing trend in the heat transfer coefficient as the frequency increases. These works covered a frequency range from 0.05 to 8 Hz.

Flow pulsation in non-tube flow was also investigated both analytically and experimentally by various researchers. Experimental study for the heat transfer coefficient of an impinging air jet to plate was reported by Sailor et. al [38]. As much as 50% of enhancement in the heat transfer coefficient was observed over a range of pulsation frequencies from 20 to 60 Hz. This finding was verified by the numerical simulation results reported by Peng et. al [39]. In their simulation of an impinging air jet on a plate, a maximum amount of enhancement of 20% was achieved.

Experimental Work - Effect of Pulsation Amplitude

Pulsation amplitude represents the difference between the average velocity and the maximum velocity of the flow. Baird et. al [22] reported positive effect of pulsation amplitude on the heat transfer coefficient of water flow in a vertical tube. Mackley et. al [33] tested water flow in a vertical tube with baffles. They found that the heat transfer coefficient increased with the product of frequency and amplitude. Chen et. al [32] who tested two-phase R-134a in water heated tubes with a range of amplitude from 10% to 30% of the average mass flux, reported that the amplitude had no noticeable effect on heat transfer coefficient

1.2.2 Pressure Drop in Pulsating Flow

The pressure drop response in pulsating flow was also investigated by various researchers. Ackerberg et. al [40] reported the measurement of pressure drop variation in time domain for single phase liquid horizontal tube flow in a tube subjected to sinusoidal wave agitation actuated mechanically. They found that the mass flow rate response starts to show second harmonic as the pulsation amplitude increases while the pressure drop response largely remains in pure first harmonic. Balakrishnan et. al [41] also carried out experimental studies on the pressure drop response to a mechanically actuated vertical tube flow. Their work showed that the magnitude of the pressure drop variation to a sinusoidal displacement profile in the vertical direction is almost linearly related to the magnitude of the variation in acceleration. It was also shown in their work that the mean pressure drop is strongly correlated to the Reynolds number of the flow. Gao et. al [42] investigated the pressure drop response of liquid flow in a vertical tube, the flow rate of which was subjected to a sinusoidal variation in pump speed. It was shown that the magnitude of variation in the Reynolds number of the flow is linearly correlated to the amplitude of pressure drop variation over the test section. In the current work, both experimental and modeling work for pressure drop response in time domain for a pulsating two-phase flow is reported.

1.3 Scope of This Work

In this work, a systemic research on pulsating flow has been conducted using both experimental and modelling approach. Effects of pulsating flow on both flow dynamic and thermal response are investigated, and the mechnism of such effects are discussed too.

Two-phase pulsating flow is investigated with an air-refrigerant evaporator, both heat transfer and pressure drop are measured under different conditions, including mass flux, inlet vapor quality, air flow velocity, pulsating period. Pulsating flow regime is also observed through a high speed camera, and the factors which might be important in heat transfer and pressure drop are addressed. Simi-emperical models for both heat transfer coefficient and pressure drop prediction are developed based on the quasi-steady assumption, the models can predict the results within an reasonable accuracy, and it can be coupled with the existing flow boiling models and very easy to apply.

This work provides a profound understanding of pulsating flow, the mechanism of heat transfer enhancement, presure drop and flow regime development. The semi-emperical model can predict pulsating flow heat transfer and pressure drop based on the steady continuous flow with a reasonable accuracy. It is the first easy-to-use model for pulsating flow.

2 Experimental Approach and Test Facility

When a flow pulsates with a prescribed period which is - in the current study, controlled by a timed solenoid valve, the mass flow rate and other parameters are expected to manifest the same periodicity. In these experiments the mass flow rate in the evaporator ideally varies periodically as shown in Figure 1, where the pulsating flow period and the on-time ratio are denoted as τ and μ. The on-time ratio μ is the ratio of on-time to the duration of the entire period. During one period, the mass flow rate is m_r during the on-time of $\mu\tau$ and 0 for the off-time of $(1-\mu)\tau$. The time-averaged mass flow rate is equal to μm_r, which will be considered as the continuous-flow baseline for comparison purpose. If μ=0.5, the on-time is equal to the off-time in a period. And during the on-time the mass flow rate for pulsating flow is set to be twice that of the continuous flow baseline. For experimental control and operation, two identical loops were created, each connected in-line with one identical evaporator. Downstream from both evaporators, refrigerant flowed into a common flow-conditioning module, consisting of a condenser, a pump, and a preheater. Just upstream of the evaporators, the flow splits and the refrigerant flow was directed into one evaporator or another, as determined by the state of the solenoid valves. When one solenoid valve was open, the other was close (see Figure 2). In this way, the flow through the shared portion of the loops was steady, but the flow through the evaporators was pulsating, and when pulsation occurred the pressure upstream of the solenoid valves was essentially constant. During the experiment, the two loops were operated alternately; there was always one loop open and one loop closed. Referring again to Figure 1, when HX1 experiences on-time, HX2 experiences off-time, and when HX1 is off, HX2 is on. The two loops are never closed at the same time. This operating procedure ensured a steady state inlet pressure and a continuous mass flow rate.

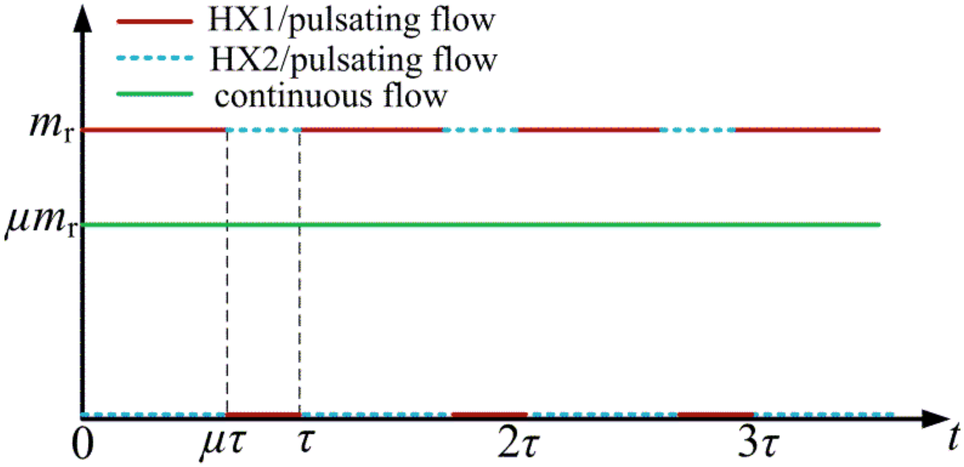

Figure 1 Pulsating flow mass flow rate vs time

The experiment apparatus is designed to measure heat transfer coefficient and pressure drop for pulsating and continuous flow, and in addition to the two refrigerant loops, there is a chilled-water loop operated at steady state to cool the condenser (see Figure 2). The two-phase flow is also observed through a glass U-bend tube by a high-speed camera, together with the observed flow regime, heat transfer and pressure drop of pulsating flow is compared with continuous flow and the mechanism will also be discussed.

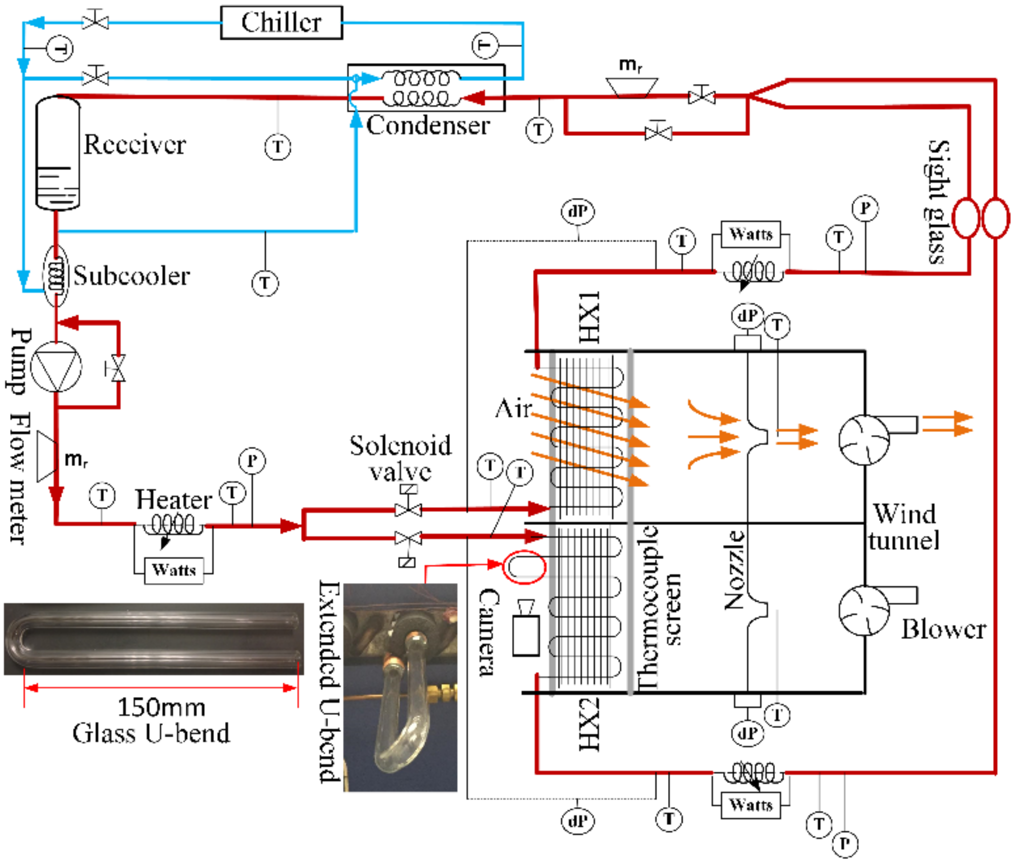

Figure 2 Schematic of the experimental setup

2.1 Test Facility

The test facility includes the fluids circulation lines, the test section, flow visualization sections and the data acquisition system. It is described in detail in the following section. There are three separated loops: the refrigerant loop (red), the chiller loop for cooling (blue) and the air loop for heating (orange), as shown in Figure 2.

2.1.1 The Refrigerant Loop

The refrigerant was driven by a variable speed pump. The flow rate of the refrigerant was measured by a Coriolis flow meter connected in-line with the pump. The refrigerant was then heated to two-phase state with a specific vapor quality using an electric heater. A schematic of the heater structure was shown in Figure 3. The pressure of the refrigerant at the inlet of the preheater was measured by a pressure transducer. A type T thermocouple was soldered at the outlet of the preheater with its measuring junction inserted through an orifice on the tube wall to measure the temperature of the refrigerant flow at that point. The total power input of the preheater was calculated using the voltage applied and the electric resistance of the heater body.

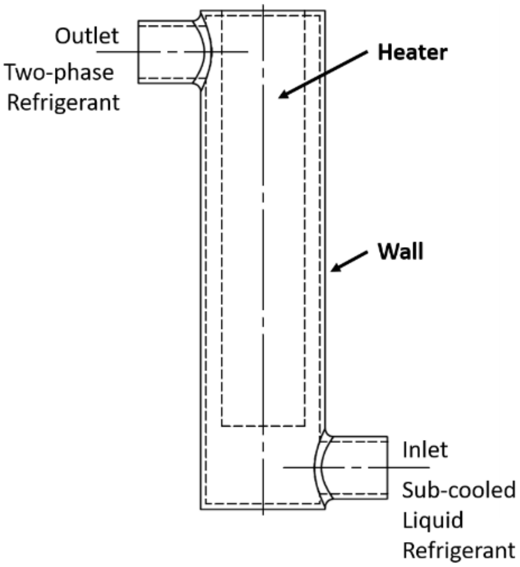

Figure 3 Schematic of the preheater

The refrigerant flow then went through a “wye” junction that splits the flow into two identical subloops. Each subloop consisted of a copy of the same test section, the same wind tunnel and the same super-heater and they merge at the same outlet that led to the condenser. The inlet of both subloop was controlled by a two-way solenoid valve that acted as a flow shutter. These two valves were programmed to operate alternately at variable frequencies. Because the valves were designed to either open or shut completely, the refrigerant flow from the pump only went into one subloop for all times.

After the solenoid valves, the refrigerant flow run through the test section (described in detail in Chapter 2.2) which was heated using air flow at the room temperature. The pressure drop in the test section was measured using a differential pressure transducer.

After the test section, a super-heater with the same construction of the preheater was installed to each subloop for heating the refrigerant to certain level of superheat, so that the enthalpy of the refrigerant flow at the outlet of the test section could be determined using the energy balance equation (discussed in detail in the data reduction section). The refrigerant then went to the condenser to be cooled, which consist of two brazed plate heat exchangers connected in series and coupled to an external chiller.

2.1.2 The Chilled Water Loop

The chilled water loop (blue loop in Figure 2) is to cool the refrigerant to sub-cool before it enters the pump. The working fluids is water-ethylene-glycol mixture. The chilled loop has the lowest operation temperature of ~15°C and cooling capacity of ~ 4 kW.

2.1.3 The Air Loop

The air loop (orange in Figure 2) consists of two separate but identical wind tunnels, which was constructed in compliance with ASHRAE standards for air flow rate measurement. The test section (heat exchanger) is in the wind tunnel, with thermocouple screen installed in the upstream and downstream of the air flow. The air blower is placed at the outlet of each tunnel pulling air downward and the converging nozzle is used to regulate air flow and together with the differential pressure transducer to measure air flow rate for each separate loop.

The temperature of air flow before and after it pass the heat exchanger were measured by type T thermocouples through the thermocouple screen. The upstream air temperature was measured by nine thermocouples. The downstream air temperature was measured by eighteen thermocouples that were placed immediately below the test section. One more thermocouple was placed at the exit of the converging nozzle. The average of the temperatures at the test section outlet and the nozzle outlet was used as the overall outlet temperature of the air flow.

The range and accuracy of tested parameters in all three loops are listed in Table 1.

Table 1 Range and accuracy of measurements (Wang et al. 2016)

Fluid	***Measurement***	***Range***	***Accuracy***
Air	Temperature [°C]	-10 to 80	±0.1
	Pressure Drop [kPa]	0 to 0.623	±1% FS
Refrigerant	Mass Flow Rate [g/s]	0 to 18	±0.1% RS
	Temperature [°C]	-10 to 80	±0.1 °C
	Pressure (inlet of HX) [kPa]	0 to 1034	±0.25% RS
	Pressure (outlet of HX) [kPa]	0 to 689	±0.25% RS
	Pressure Drop [kPa]	0 to 37.36	±0.25% RS
	Heater Power [W]	0 to 1000	±0.02 W

2.2 Test Section and Flow Visualization

The test section is a single pass copper tube coil with a 6.2 mm inside diameter and 8.5 mm external diameter. It has a staggered tube arrangement. The tube has a total length of 2.18 m, brazed with plain fin made of 0.3 mm thick aluminum foils with a fin density of 15 fins per inch. The dimensions were summarized in the table below:

Table 2 Dimension and layout parameters of the tube and fin in the heat exchanger

Tube Configuration	**Tube Details**	**Fin Details**
Single Pass, Staggered	Round, Smooth	Plain Fin
Two Rows	Copper	Aluminum
Length, Width, Thickness	*O.D* = 8.0 mm	Fin Density = 15 fpi
385×300×30mm	*I.D* = 6.2 mm	Fin thickness = 0.3 mm

Visualization sections are made of U-bends made of glass with a length of 150 mm installed and replaced some original copper U-bends of the heat exchanger with identical inside diameter as shown in Figure 4. Flow inside the sight glass was captured using a high-speed camera placed either above or at the side of the glass tubes, and the object was illuminated using one 100 watts LED lamp powered by DC current which eliminated the 60 Hz fluctuation while using the AC power (see Figure 4). The model of the camera is Phantom Miro 310. Its maximum frame rate is 10,000 fps and the maximum resolution s 1280×800. The camera is used in combination with a prime lens, which has a focal length of 105mm and maximum aperture of f2.8. However, due to the limitation in the shooting angle, only the image for the first glass U-bend could be captured in the current stage.

Figure 4 Test Section with Glass Tubes

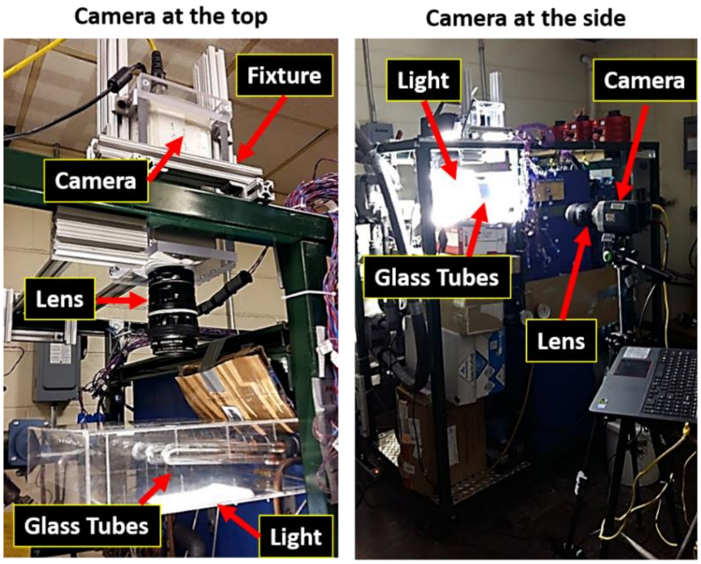

Camera at the top

Camera at the side

Figure 5 Placement of the camera and the light source

2.3 Data Acquisition

An Agilent 34980A main frame was used to log the voltage signals from thermocouples and pressure transducers. The voltage signals were measured using Agilent 34921A armature type multiplexers via 34921T terminal blocks. The reference junctions for the thermocouples were immersed in a thermal bath filled with thermal paste kept at room temperature.

Data logging was performed using a desktop computer interfaced with the Agilent34980A main frame with Agilent VEE Pro 6.0 software. The camera control software used in flow regime visualization is made by Vision Research. Some images captured were synchronized with the pressure drop measurements by utilizing the external trigger function built-in with the camera control module. A custom made low voltage electric switch was connected to the triggering port on the camera and an input port on the data acquisition board. When the switch was closed, both the camera control software and the data acquisition board received the low voltage signal so that the image capture and data acquisition started simultaneously. The data acquisition program ran at a given time interval and the images captured contained time information, so that the correspondence between the data and image could be determined.

2.4 Description of the Tests

The tests matrix included over 450 tests. Each test is grouped by several time-average flow parameters including the mass flux, vapor qualities, and air temperature and flow rates. Each group consists of one continuous flow test and several pulsating flow tests with different pulsation periods. All the tests in the same group had the same saturation temperature, mean mass flux and inlet vapor quality for the refrigerant flow. A constant inlet temperature and flow rate for the air flow is also maintained for tests in each group, because any meaningful comparison between the continuous and pulsating flow needs to be made at the basis of constant environmental parameters. Each step of adjusting the equipment to make the system reach the desired operating parameters can be found in the following descriptions:

1. Determine the mean flow parameters for the test, i.e. mean mass flux, inlet and outlet vapor quality for the refrigerant flow.

2. Adjust power of all equipment to make the system reach steady state with the desired mass flux, inlet and outlet vapor quality for the refrigerant.
3. Record data after parameters stabilize.
4. Keep the air blower power and the ambient air temperature constant for the rest of the tests.
5. Turn on the timer. Set the timer to two seconds with 50% duty cycle to enable the pulsation mechanism. Increase the pumping power to reach double the mass flux from the pump (see Figure 1). Adjust the heater power to keep the inlet vapor quality of the refrigerant flow consistent with that of the continuous flow test.
6. Record data after parameters stabilize. Increase the timer cycle to four seconds. And repeat step five.
7. Record data after parameters stabilize. Increase the timer cycle to six seconds. And repeat step five. And so on for the other pulsation periods tested.

2.5 Test Matrix

All working conditions tested were organized using the test matrix shown in the table below. The equivalent mass flux was the same as the time-averaged mass flux.

Table 3 Test Matrix

Equivalent Mass Flux [kg/m^{2}s]	**Inlet Vapor Quality (%)**	**Outlet Vapor Quality (%)**
75	10-20	80-90
100	10-50	50-90
125	10-30	60-80
150	10-50	60-90
175	10	80
200	10-50	30-80
250	40	80

For each set of tests that had the same equivalent mass flux, inlet and outlet vapor qualities, continuous flow and pulsating flow with a pulsation period of 2, 4, 8, 12, 16, 20, 24 seconds were all tested. Although the air flow rate and air temperature were kept constant throughout the same set of tests, the final outlet vapor quality may vary depending on the overall heat transfer coefficient of the flow.

3 Experimental Results and Discussion

3.1 Experimental Data Reduction Methods

The data necessary to calculate the heat transfer coefficient were obtained as above described. The experimental time-averaged overall heat transfer coefficients at the refrigerant to tube-wall interface were calculated using LMTD method using the following equations:

$$Q = UA \cdot F \cdot LMTD \tag{5}$$

where Q = time-averaged total heat flow rate through the test section [W]

UA = the overall heat transfer coefficient [W/K]

F = correlation factor for logarithmic mean temperature difference for the type of heat exchanger used in the test section

LTMD = logarithmic mean temperature difference [K] between tube wall and refrigerant = $\frac{\Delta T_1 - \Delta T_2}{log_{10}\left(\frac{\Delta T_1}{\Delta T_2}\right)}$ where ΔT_1 and ΔT_2 are initial and final temperature difference

$\Delta T_1 =$ Temperature difference between the temperature of the air flow at the inlet and the saturation temperature of the refrigerant flow at the inlet

$\Delta T_2 =$ Temperature difference between the temperature of the air flow at the outlet and the saturation temperature of the refrigerant flow at the outlet

Once the overall heat conductance from air to refrigerant, UA is obtained, the heat transfer coefficient from the refrigerant to tube wall surface h [W/m^2-K] can be expressed in the following equation:

$$h = \frac{1}{A_r} \cdot \left(\frac{1}{UA} - R_a - R_c - \frac{1}{h_c \cdot A_r} \right)^{-1} \tag{6}$$

where A_r= total tube-wall surface in contact with refrigerant flow [m^2]

$R_a =$ thermal resistance at the air side = $(\eta \cdot h_a \cdot A_a)^{-1}$ [K/W]

η = fin efficiency

h_a= air side heat transfer coefficient [W/m^2-K]

A_a= air side surface area [m^2]

R_c = thermal resistance of the tube material = $\frac{ln\left(\frac{r_o}{r_i}\right)}{2\cdot\pi\cdot k_{copper}}$ [K/W]

r_o = outside radius of the tube, 4.0 mm

r_i = inside radius of the tube, 3.2 mm

k_{copper} = thermal conductivity of copper [W/m-K]

h_c = contact heat transfer coefficient between fin and tube[43] = 9.5 kW/m^2-K

A_r = inside surface area of the tube [m^2]

The fin efficiency η was calculated based on the rectangular fin correlation for staggered tube bundle proposed by Hong and Webb [44]. The equations are included in appendix B. The air side heat transfer coefficient h_a was estimated using the correlation proposed Kim et. al [45] developed for plain fin-and-tube heat exchangers with a staggered tube configuration. The detailed formulations are given in appendix C.

3.2 Experimental Results and Analysis

The focus of this analysis is to show how the flow parameters affect the pulsating flow heat transfer coefficient, pressure drop and flow regime. The flow regime results are further used to explain the enhancement of heat transfer with pulsating flow.

3.2.1 Heat Transfer Coefficient

The time-averaged refrigerant side heat transfer coefficient for continuous and pulsating flow was plotted against the pulsation period in Figure 4 to Figure 13. Data points within each figure were separated by the inlet and outlet vapor qualities. In each sub figure, the heat transfer coefficient data were plotted on the *y*-axis and the pulsation period on the *x*-axis. It shall be pointed out that results for continuous flow are plotted on the position where the pulsation period equals zero second.

As shown in Figure 4, the heat transfer coefficient increases in pulsating flow at short pulsation periods. To better demonstrate the comparison between pulsating flow and continuous flow, the definition of enhancement ratio was employed, which is written as：

$$\text{HTC Enhancement Ratio} = \frac{h_{\text{pulsation}}}{h_{\text{continuous}}} \tag{7}$$

Results for the heat transfer coefficient plotted in Figure 4 can then be converted into the scale of HTC enhancement ratio, which were plotted in Figure 5. Through an inspection of Figure 4 to Figure 13, it was noted that the enhancement ratio decreases with the pulsation period. The largest enhancement in heat transfer for each different mass flux level was mostly found at two seconds pulsation period (see Figure 5, Figure 7, Figure 9, Figure 11 and Figure 13).

For tests with a mass flux of 200 kg/m^{2}s, a substantial rise in the heat transfer enhancement ratio was found in two cases, vapor quality range = 0.1 to 0.3 and 0.3 to 0.5 (see Figure 13). The maximum enhancement ratio for those two cases were 248% and 169% both found at the two second pulsation period.

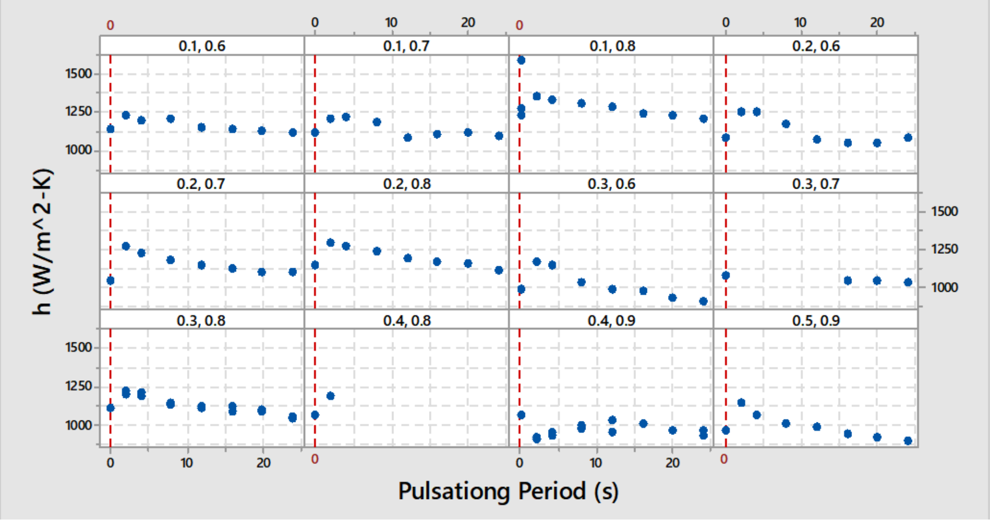

Figure 4 Refrigerant side heat transfer coefficient grouped with different vapor quality range plotted against the pulsation period for G=100 kg/m^{2}s.

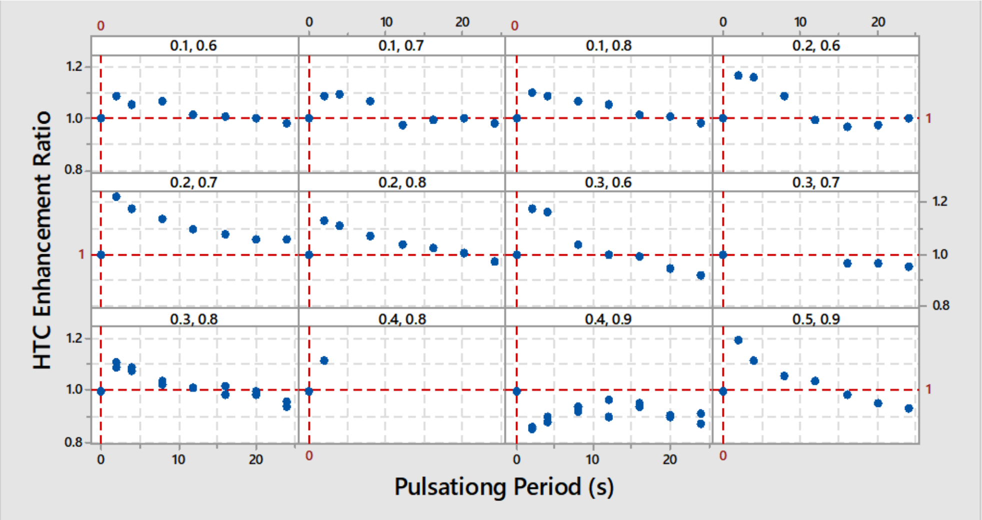

Figure 5 Enhancement ratio of refrigerant side heat transfer coefficient grouped with different vapor quality range plotted against the pulsation period for G=100 kg/m^{2}s.

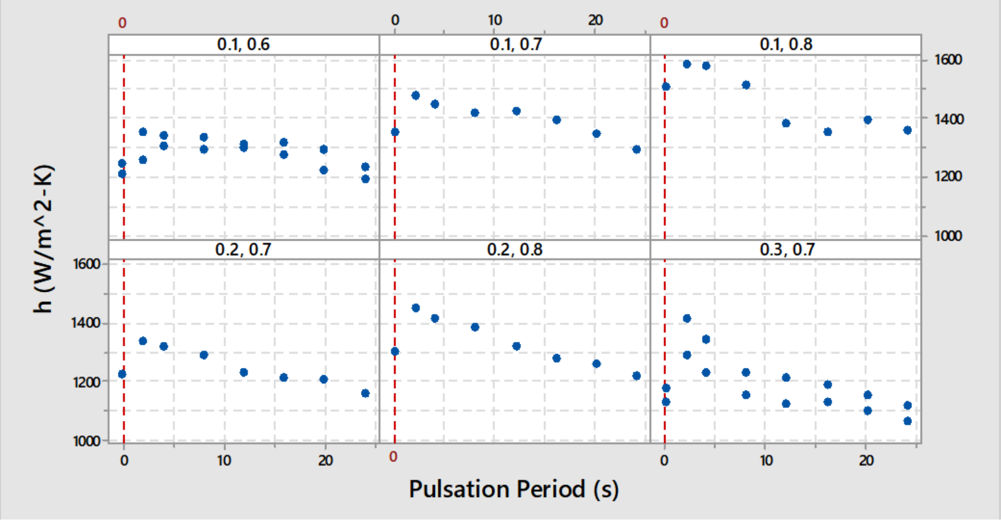

Figure 6 Refrigerant side heat transfer coefficient grouped with different vapor quality range plotted against the pulsation period for G=125 kg/m^2s

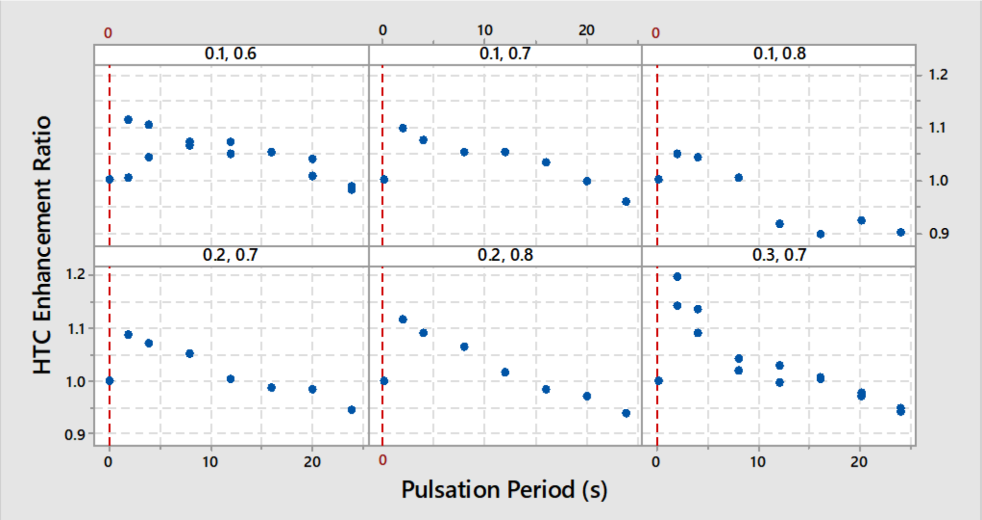

Figure 7 Enhancement ratio of the refrigerant side heat transfer coefficient grouped with different vapor quality range versus pulsation period for G=125 kg/m^2s.

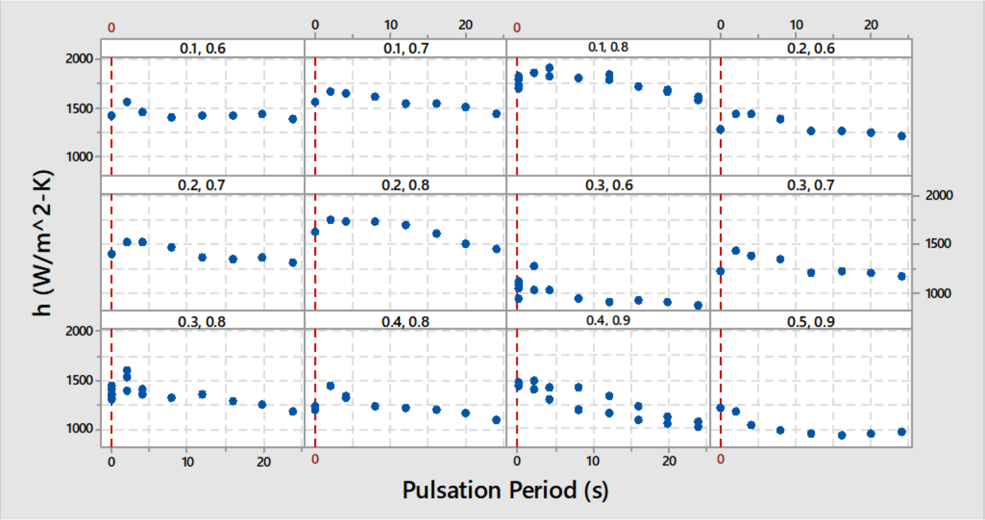

Figure 8 Refrigerant side heat transfer coefficient grouped with different vapor quality range plotted against the pulsation period for G=150 kg/m^{2}s.

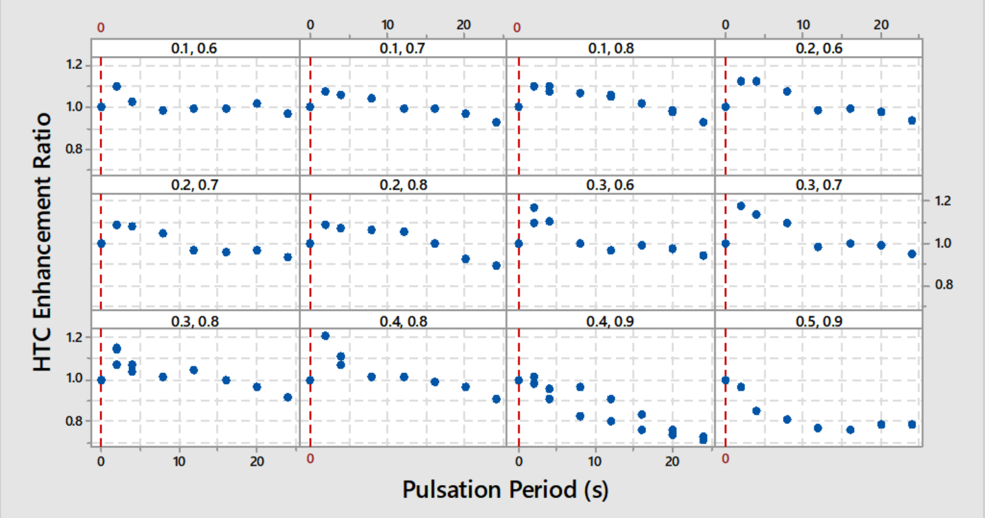

Figure 9 Enhancement ratio of the refrigerant side heat transfer coefficient grouped with different vapor quality range versus pulsation period for G=150 kg/m^{2}s.

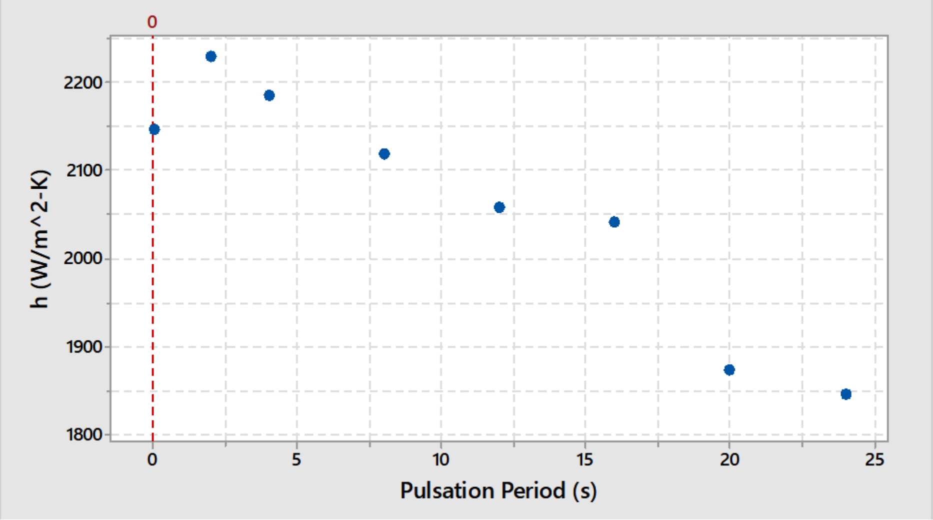

Figure 10 Refrigerant side heat transfer coefficient grouped with different vapor quality range plotted against the pulsation period for G=175 kg/m^{2}s.

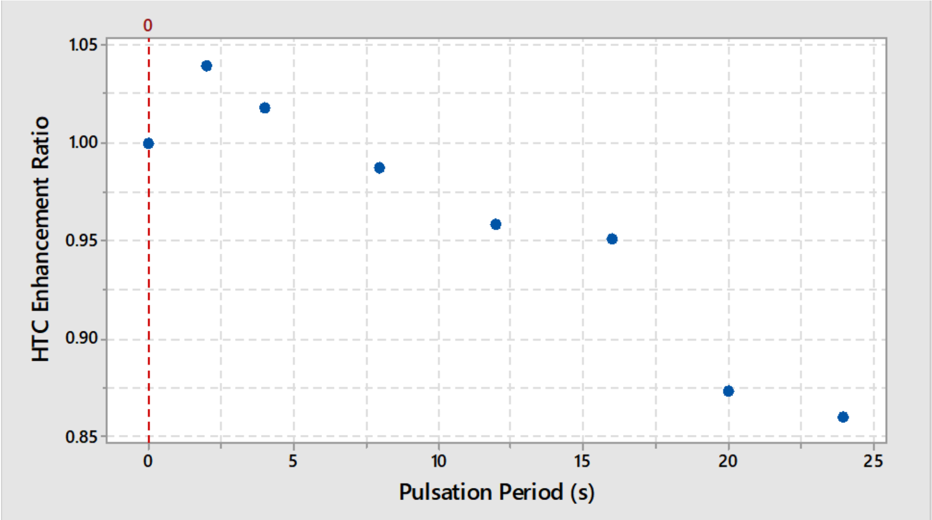

Figure 11 Enhancement ratio of the refrigerant side heat transfer coefficient grouped with different vapor quality range versus pulsation period for G=150 kg/m^{2}s.

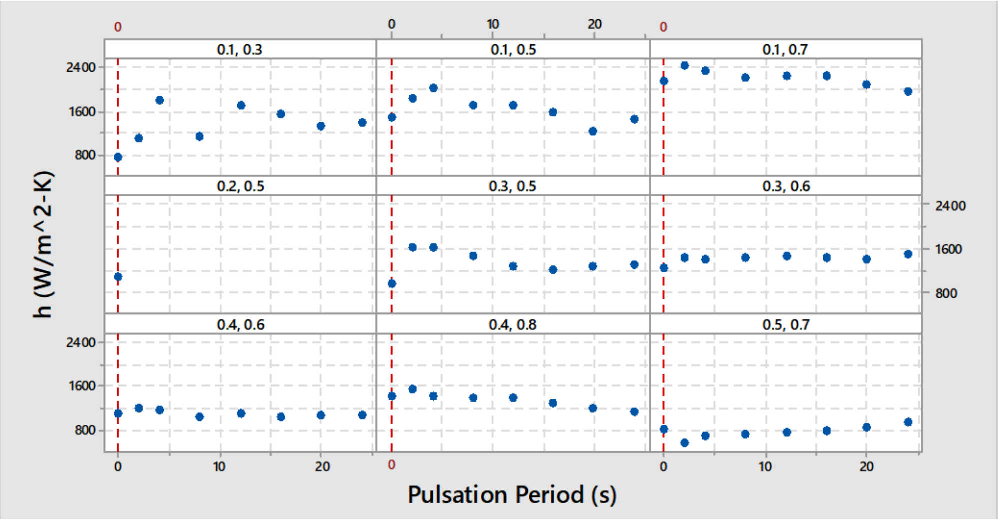

Figure 12 Refrigerant side heat transfer coefficient grouped with different vapor quality range plotted against the pulsation period for G=200 kg/m^{2}s.

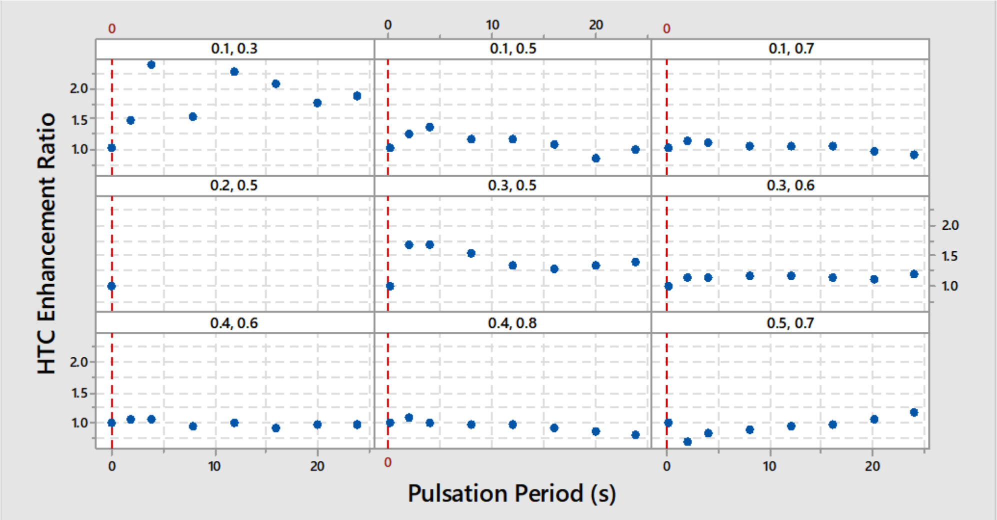

Figure 13 Enhancement ratio of the refrigerant side heat transfer coefficient grouped with different vapor quality range versus pulsation period for G=200 kg/m^{2}s.

3.2.2 Pressure Drop

Time-average Pressure Drop

The time-averaged pressure drop was plotted against the pulsation period in Figure 15 to Figure 21. The data organization and graphic layout were in the same fashion as the heat transfer coefficient graphs (see Figure 4 to Figure 13). The pressure drop ratio parameter was employed to illustrate the comparison between pulsating flow and continuous flow results:

$$\text{Pressure Drop Ratio} = \frac{\Delta p_{\text{pulsating}}}{\Delta p_{\text{continuous}}}$$

It is found that the time-averaged pressure drop generally increases with the pulsation period for short periods and decreases for long periods, as shown in Figure 14 to Figure 21 . As the heat transfer enhancement was also more pronounced for lower pulsation period, it is possible to find cases where the heat transfer enhancement and pressure drop reduction coexists, which is favorable for engineering applications.

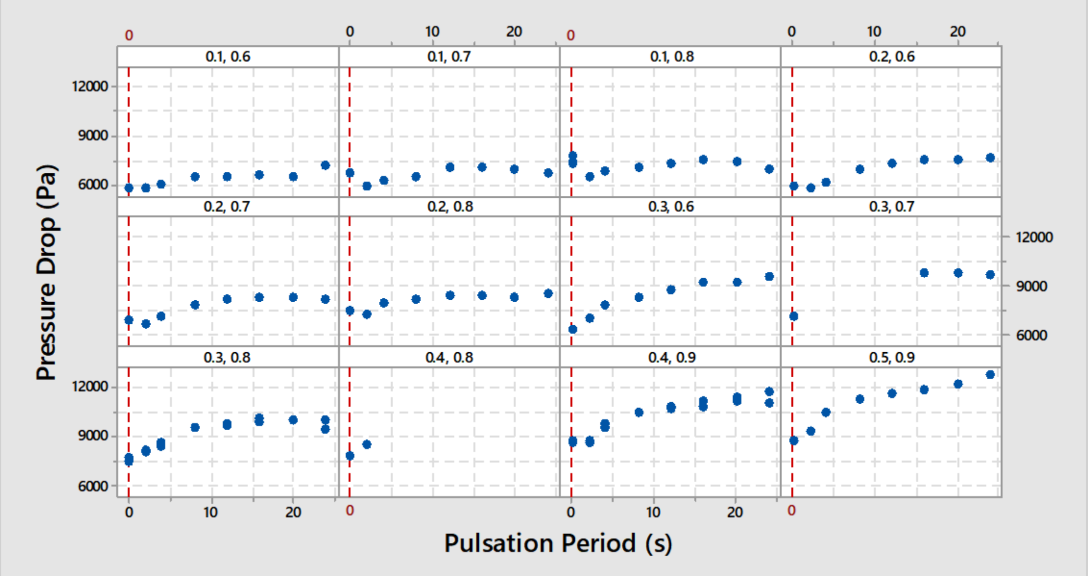

Figure 14 Pressure drop versus pulsation period for mass flux 100 kg/m^{2}s.

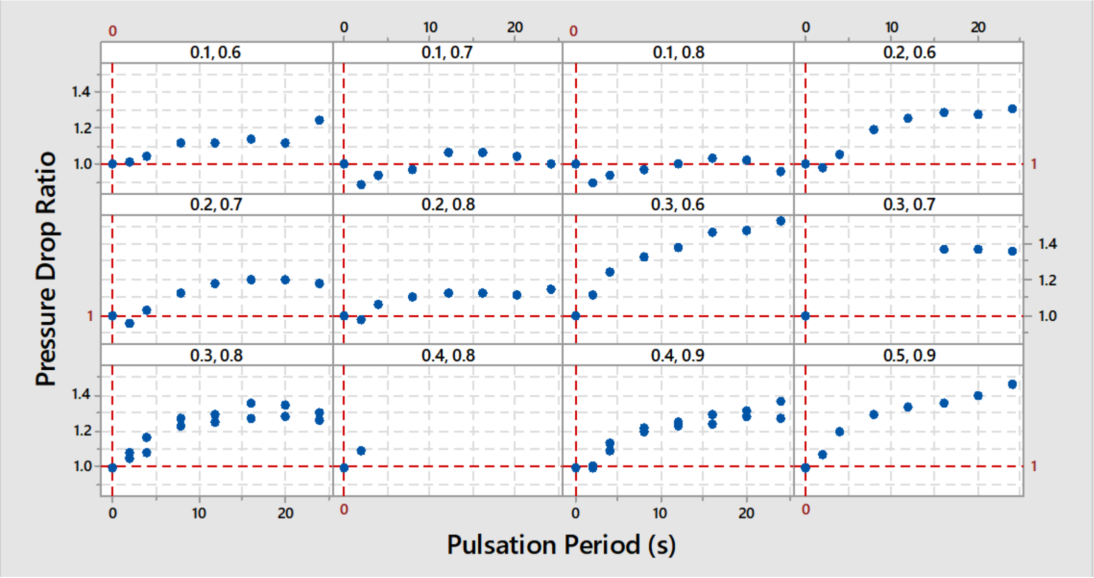

Figure 15 Pressure drop ratio versus pulsation period for mass flux 100 kg/m^{2}s.

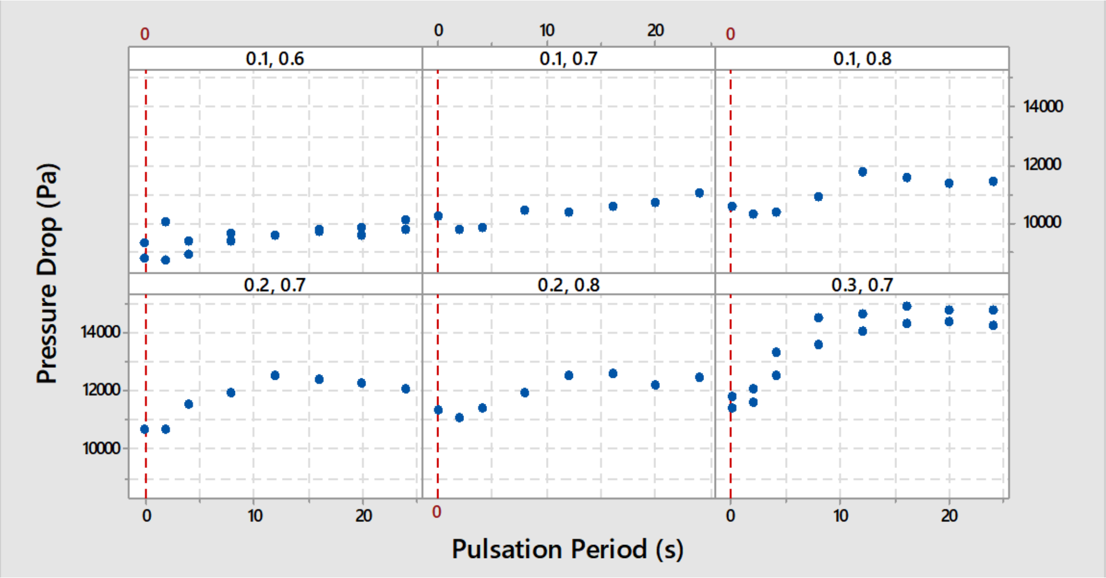

Figure 16 Pressure drop versus pulsation period for mass flux 125 kg/m^{2}s.

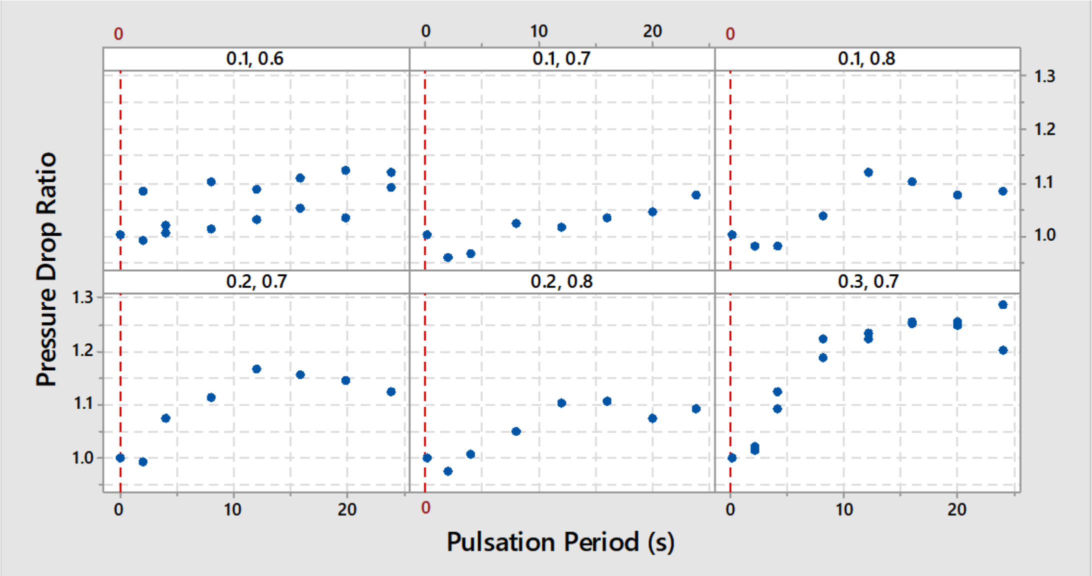

Figure 17 Pressure drop ratio versus pulsation period for mass flux 125 kg/m^{2}s.

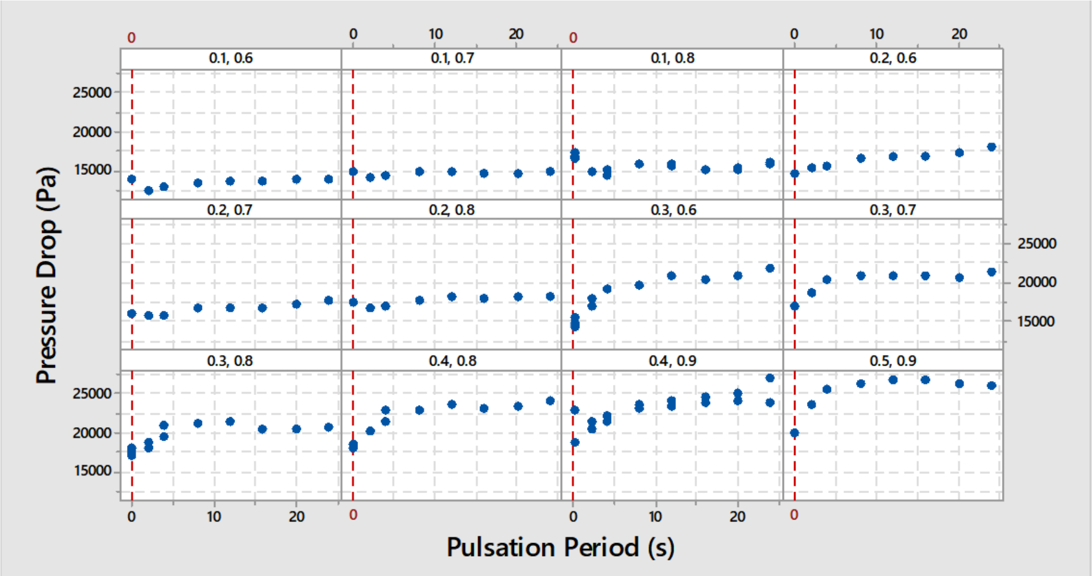

Figure 18 Pressure drop versus pulsation period for mass flux 150 kg/m^{2}s.

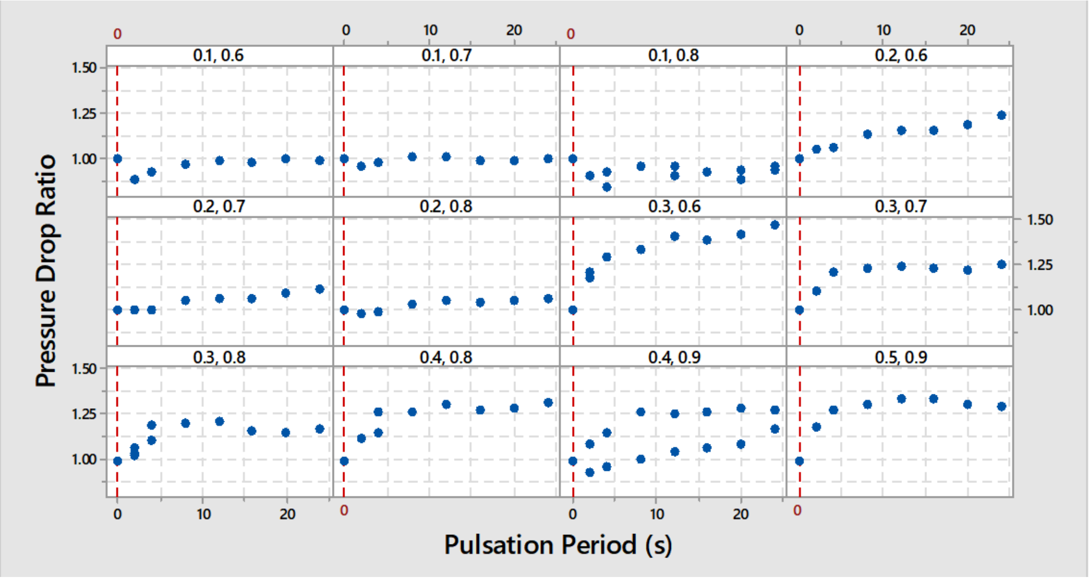

Figure 19 Pressure drop ratio versus pulsation period for mass flux 150 kg/m^{2}s.

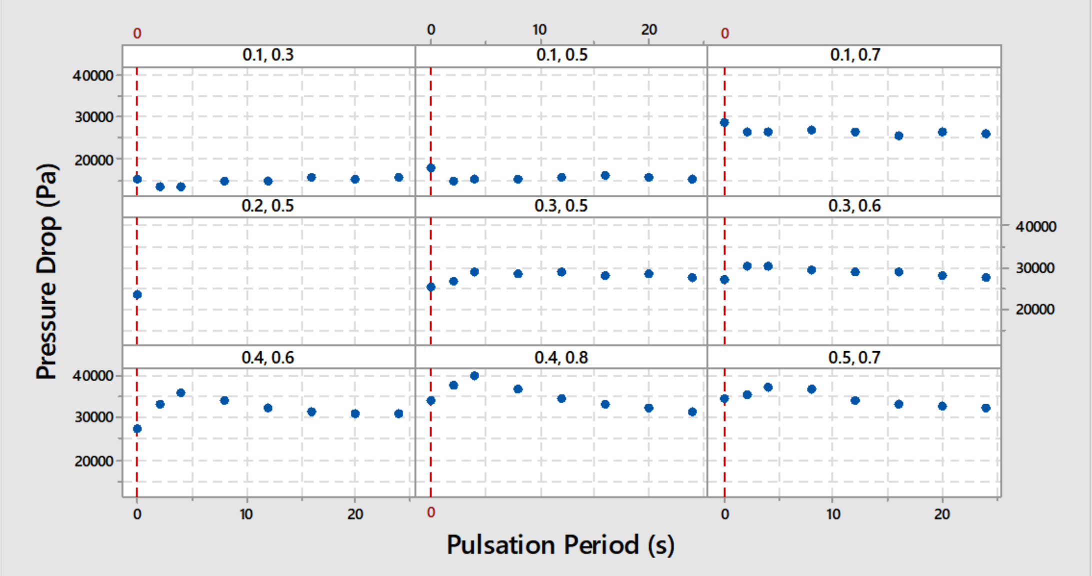

Figure 20 Pressure drop versus pulsation period for mass flux 200 kg/m^{2}s.

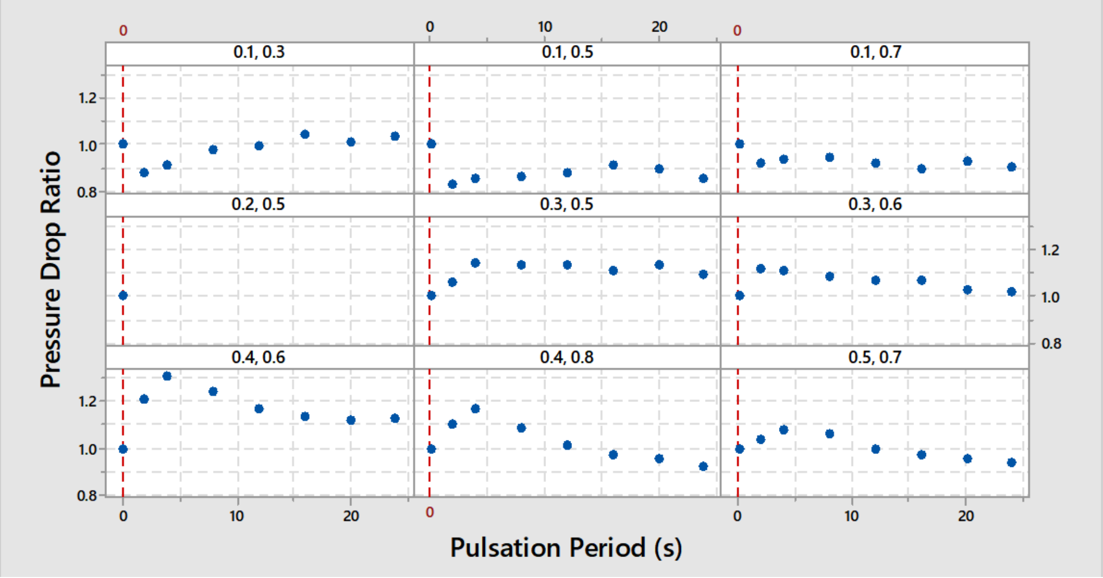

Figure 21 Pressure drop ratio versus pulsation period for mass flux 200 kg/m^{2}s.

Temporal Pressure Drop

The temporal pressure drop data taken from pulsating flow tests with a mean mass flux of 150kg/m2-s, inlet and outlet vapor quality of 0.1 and 0.8 is plotted in time-domain in Figure 22. Data from each different pulsation period is plotted separately in a sub-diagram, where the solid blue curve represents the pulsating flow data and the dashed line represents the value of the steady flow pressure drop.

It was shown that the magnitude of fluctuation in the temporal pressure drop profile increases with the pulsation period. The higher peak and lower valley in the pressure drop profile for longer pulsation periods may be caused by its longer valve on-time and off-time. During the valve on-time, the flow is constantly exposed to the pressure gradient mainly due to the velocity head at the inlet, thus as the exposure time increases, the flow velocity inside the test section constantly rises, which is causing a growing frictional pressure drop inside the test section. Furthermore, the increasing flow velocity causes a higher heat transfer between the tube and the flow, which accelerates the liquid-vapor phase change of the fluid, causing a higher accelerational pressure drop. Both higher frictional and accelerational pressure drop contribute to the increase in the peak pressure drop for test conditions with a longer pulsation period.

During the valve-off time, the velocity head at the inlet becomes zero as the valve is shut, thus the inlet mass flow also becomes zero. The remaining fluid in the test section gradually reduces in mass and velocity as it leaves the test section by inertia or boils and evaporates into vapor. Thus, the frictional and accelerational pressure drop in the test section during off-time asymptotically approaches zero with time. This explains the observed lower valley in temporal pressure drop data for longer pulsation periods.

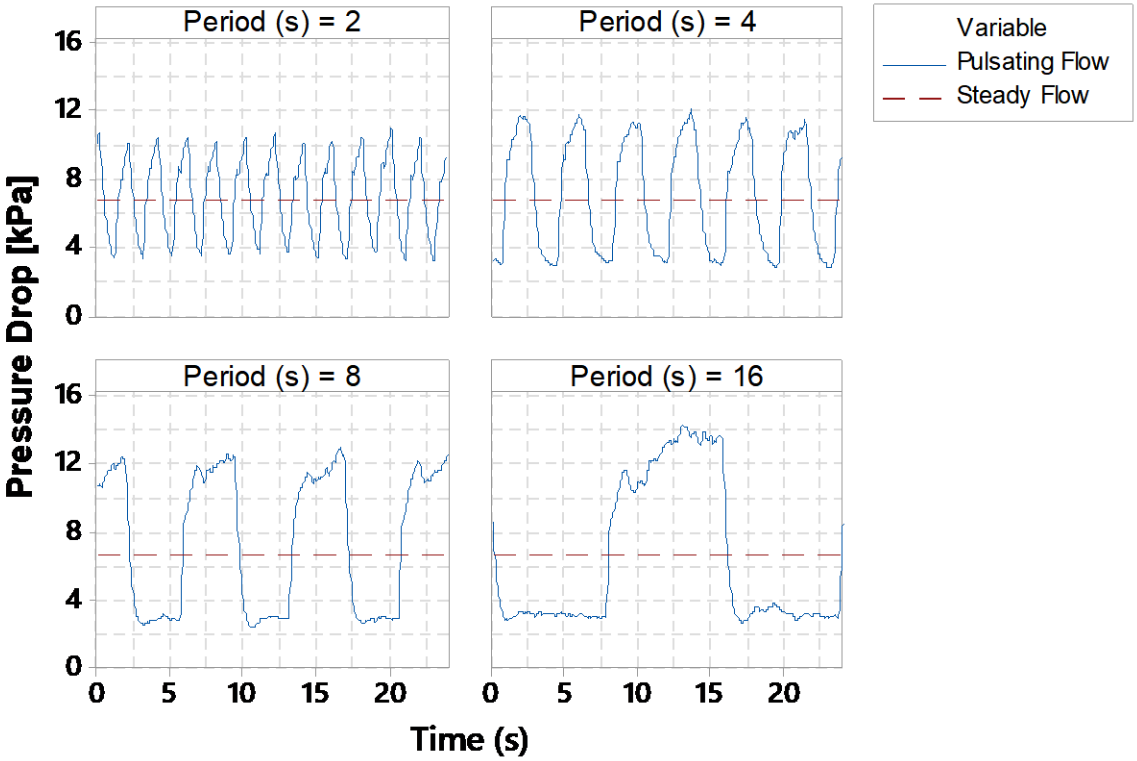

Figure 22 Pressure drop in time domain. G=150kg/m^2-s; pulsation period=2 to 16s; x=0.1 to 0.8

Effect of Pulsation Period and Vapor Quality on Both Pressure Drop and Heat Transfer

Results from Figure 4 to Figure 21 can be merged into fewer graphs by plotting the enhancement ratio of the heat transfer coefficient against the ratio of pressure drop. It became convenient to find working conditions that simultaneously performed better in heat transfer and pressure drop.

In Figure 23 to Figure 26, points in the upper left sector of the chart represents test conditions that produced a heat transfer enhancement ratio larger than one and a pressure drop ratio smaller than one. In other words, those pulsating flow test conditions produced both enhancement in the heat transfer coefficient and reduction in the pressure drop. Points in the upper right sector of the chart represents test conditions that produce a heat transfer enhancement ratio larger than one and a pressure drop ratio larger than one. These were the cases where the enhancement in the heat transfer coefficient was accompanied by an increase in the pressure drop. All the point in the lower sectors of the graphs showed no enhancement in the heat transfer coefficient. It became apparent that mainly the pulsating flow tests with an inlet vapor quality 0.1 and 0.2 showed both enhancement in the heat transfer coefficient and reduction in the pressure drop.

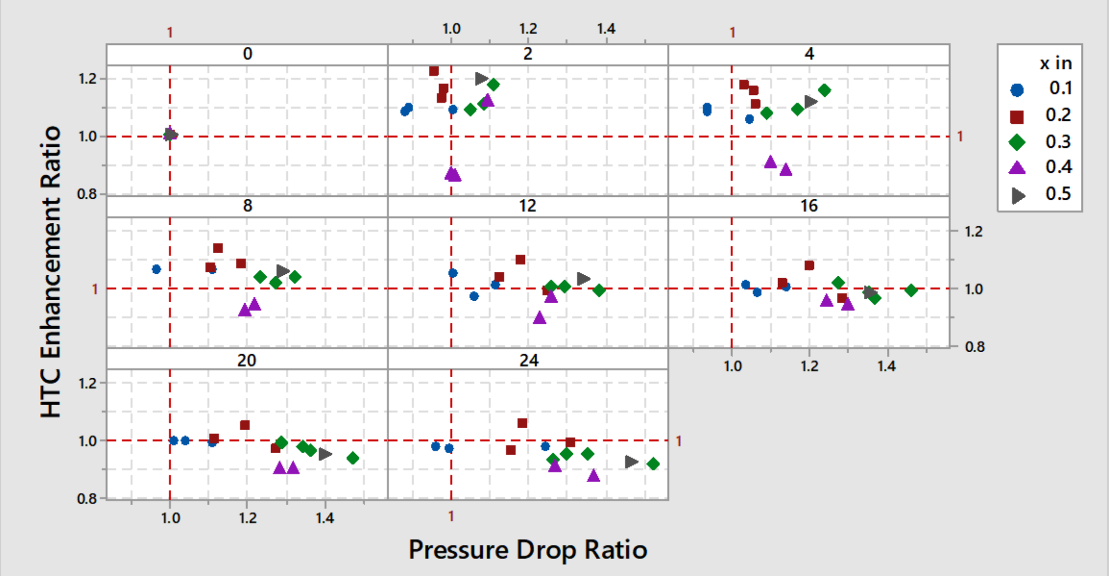

Figure 23 Enhancement ratio versus pressure drop ratio for mass flux 100 kg/m^{2}s.

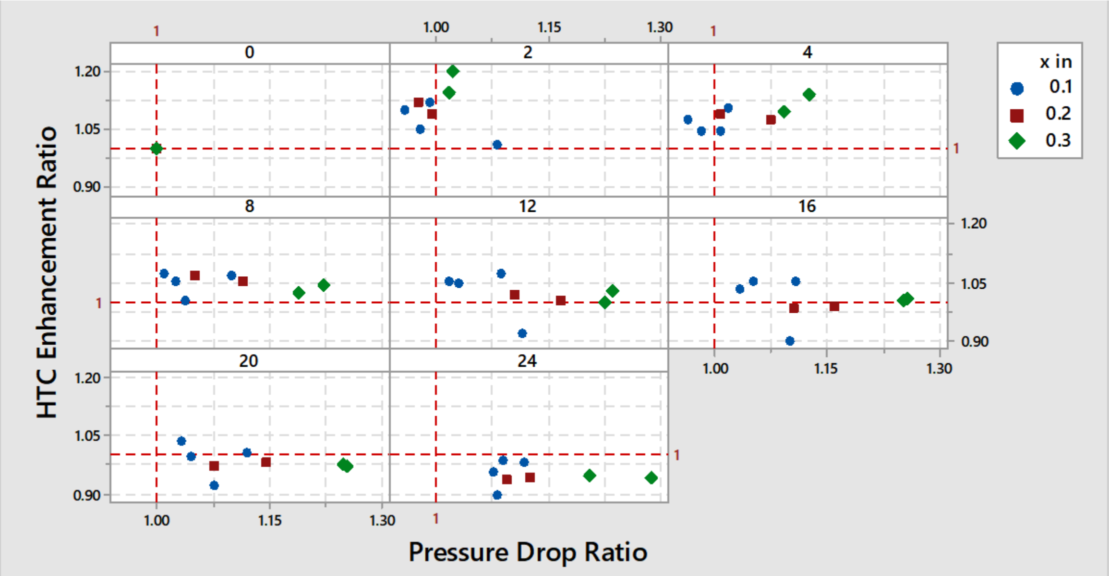

Figure 24 Enhancement ratio versus pressure drop ratio for mass flux 125 kg/m^{2}s.

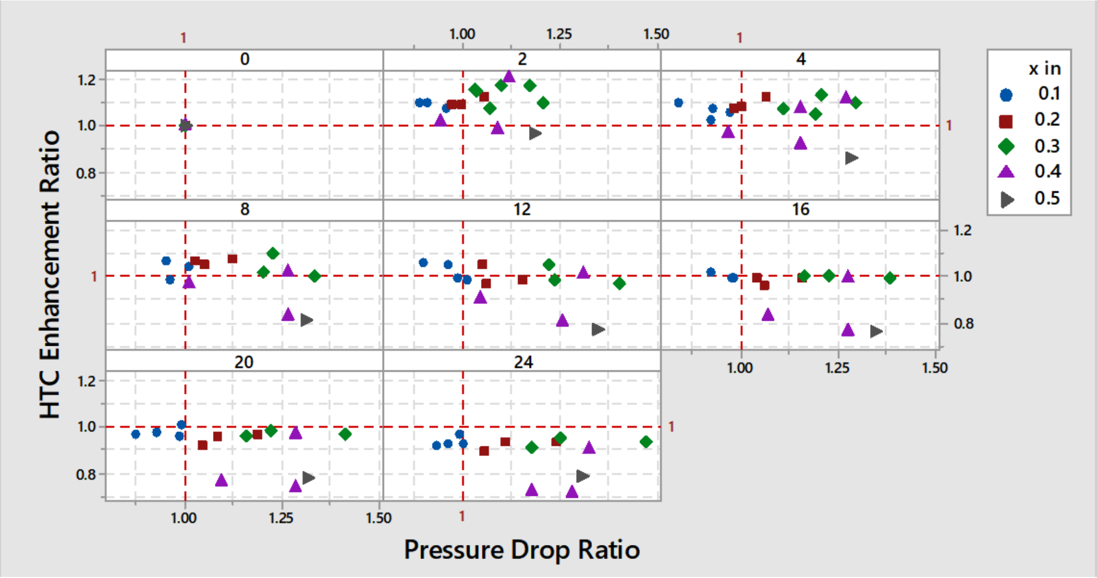

Figure 25 Enhancement ratio versus pressure drop ratio for mass flux 150 kg/m^{2}s.

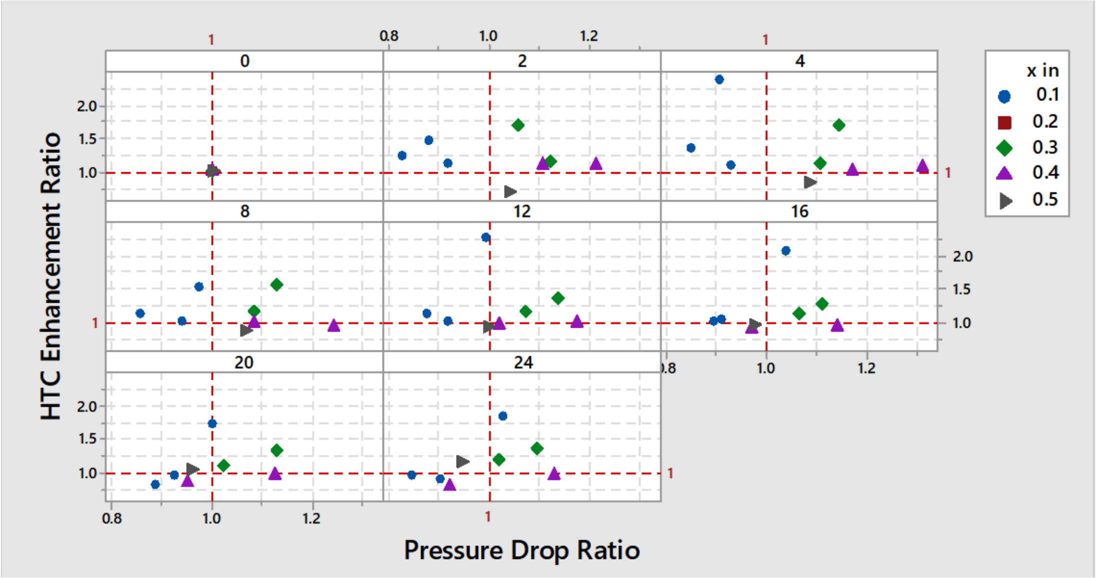

Figure 26 Enhancement ratio versus pressure drop ratio for mass flux 200 kg/m^{2}s.

Effect of Inlet and Outlet Vapor Quality on Both Heat Transfer and Pressure Drop

It is a common notion that the flow regime has a strong influence in the heat transfer of in-tube two phase flow as it dictates the effective wetting area on the tube wall. One of the flow parameters that strongly affect the flow regime of two-phase flow is the vapor quality. Several classic and recently developed flow regimes maps [46] used vapor quality as the determining parameter. Thus, it becomes natural to study the effect of vapor quality to the heat transfer and pressure drop of pulsating flow. The overall heat transfer coefficient was plotted against the inlet and outlet vapor qualities in Figure 27 to Figure 30, where the data are taken from pulsating flow tests with a mass flux of 100 kg/m^2-s and a pulsation period from 2-24 seconds. The inlet and outlet vapor quality were plotted on the *y* and *x* axis, respectively.

Through an inspection of all the four graphs, it is noticeable that the heat transfer coefficient decreases with the inlet vapor quality for a constant outlet vapor quality. The same observation was reported by Thome et. al [47] in 2005, where the heat transfer coefficient of R22 and R-410A dropped monotonically after the vapor quality exceeded 0.5. And the opposite trend was also reported by Thome et. al [48] in 1998, who showed that the heat transfer coefficient of R134a increased with the vapor quality and dropped when the vapor quality exceeded 0.8. The author suggested two explanations for the observed effect in perspectives of the heat flux and the settling time.

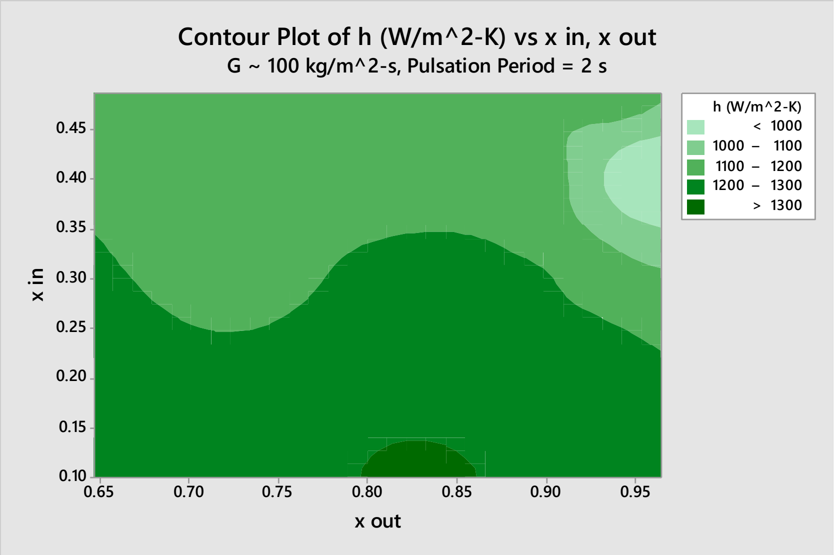

Figure 27 Refrigerant side heat transfer coefficient versus inlet and outlet vapor quality for pulsating flow, mass flux 100 kg/m^{2}s, pulsation period 2 seconds.

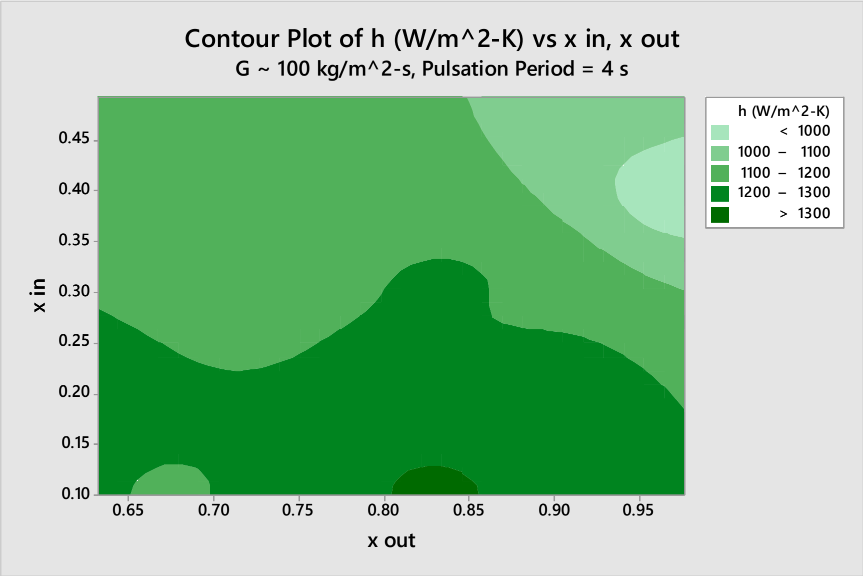

Figure 28 Refrigerant side heat transfer coefficient versus inlet and outlet vapor quality for pulsating flow, mass flux 100 kg/m^{2}s, pulsation period 4 seconds.

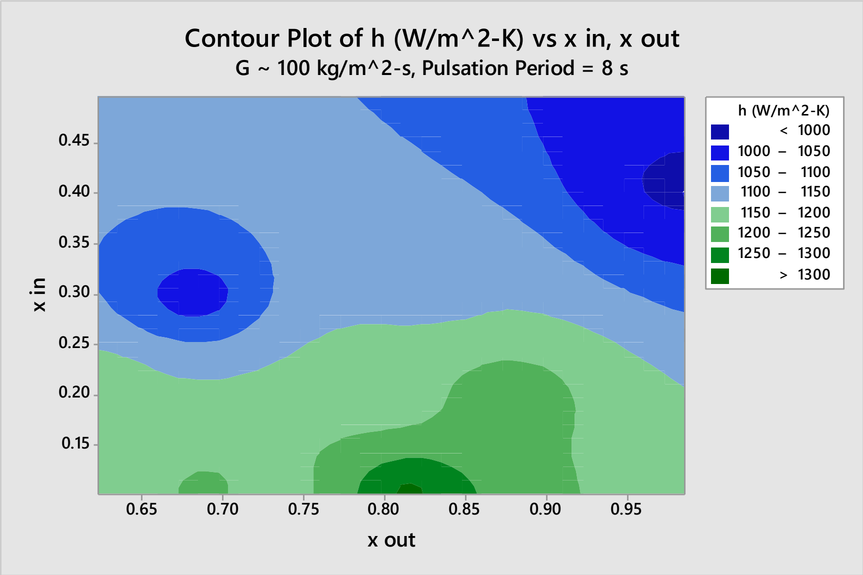

Figure 29 Refrigerant side heat transfer coefficient versus inlet and outlet vapor quality for pulsating flow, mass flux 100 kg/m^{2}s, pulsation period 8 seconds.

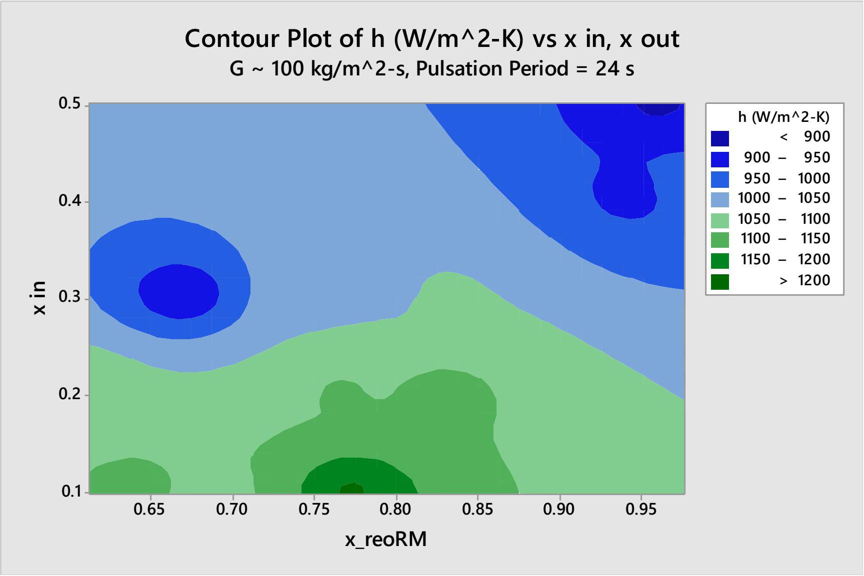

Figure 30 Refrigerant side heat transfer coefficient versus inlet and outlet vapor quality for pulsating flow, mass flux 100 kg/m^{2}s, pulsation period 24 seconds.

In the perspective of heat flux, as the inlet vapor quality increases when the outlet vapor quality was a constant, the overall heat flux applied to the heat exchanger was reduced, which resulted in a lower heat transfer coefficient.

In the perspective of the settle-down time of the flow during valve-off time, since the settle-down time is dictated by the amount of liquid and the overall velocity of the fluid existed in the tube when the solenoid valve shuts down the inlet, when the inlet vapor quality increases, the liquid content in the tube decreases dramatically, which caused the flow to evaporate and settle down much faster. This effect was observed in both pressure drop profile and the high-speed flow regime images.

In Figure 31, the pressure drop profile of the test section with a mean mass flux of 100 kg/m^2-s, pulsation period of two seconds, an inlet vapor quality of 0.1 and various outlet vapor qualities were plotted in the time domain. The zero second time point represented the moment when the solenoid valve opened and the blue dashed line at one second represented the moment when the solenoid valve closed. Through an inspection of Figure 31, it is apparent that after the valve was closed, pressure drop value settled faster with a higher inlet vapor quality. As the pressure drop of fluid flow was always positively correlated with the flow velocity, a faster settle down rate of pressure drop indicated a faster rate of drop in the flow velocity, which thus resulted in a lower heat transfer coefficient during valve off-time.

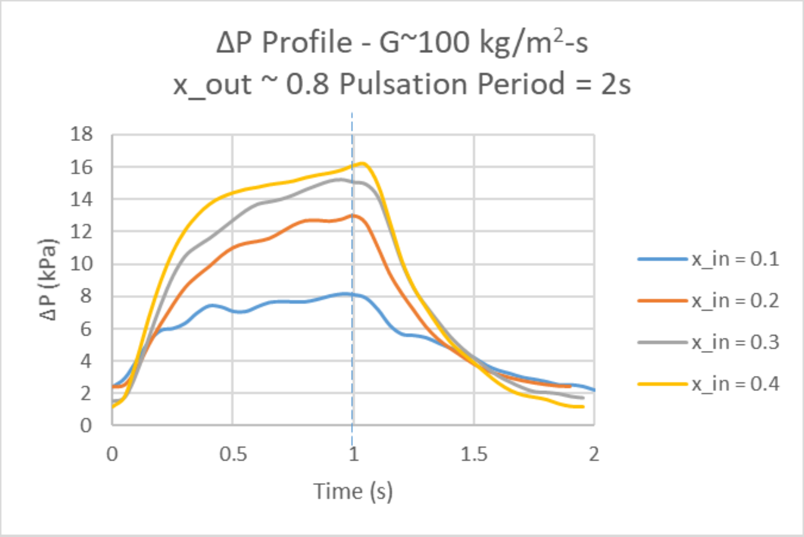

Figure 31 Temporal pressure drop variation with time for mass flux 100 kg/m^{2}s, outlet vapor quality 0.8 and pulsation period 2 seconds.

Similarly, the same effect could be observed in the pressure drop profile of tests with a mass flux of 200 kg/m^2-s, which were plotted in Figure 32.

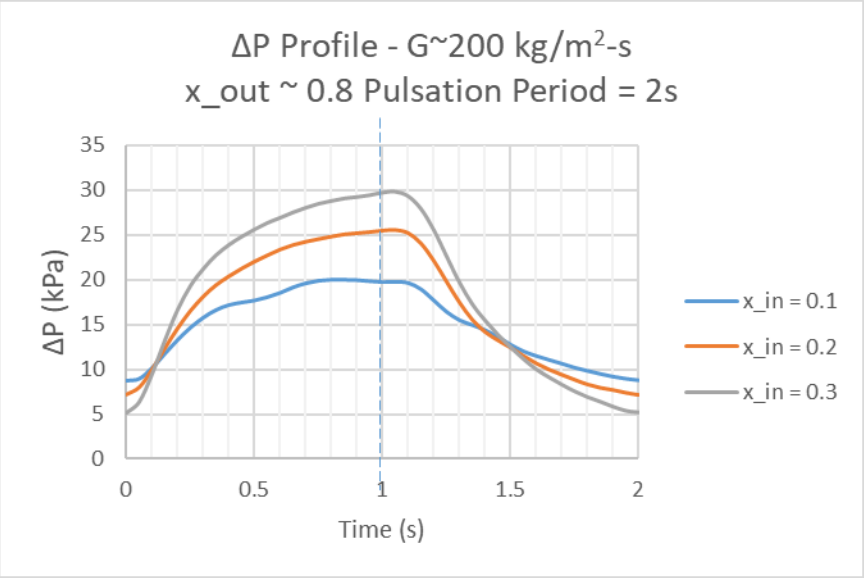

Figure 32 Temporal pressure drop variation with time for mass flux 200 kg/m^{2}s, outlet vapor quality 0.8 and pulsation period 2 seconds.

3.2.3 Flow Regime Visualization

Images of the flow regime were captured using the high speed camera at a rate of around 10,000 frames per second. With proper lighting and exposure setting, the speed can go up to 16k frames per second where more detials of the flow can be captured; however, due to the limitation of the on-board memory space and processing time, only one trial at 16k frames per second were recorded. The images are presented in Figure 33 and Figure 34.

These images were captured with the camera placed above the first glass tube from the inlet of the test section before the U-bend, where the mass flux was 100 kg/m^2-s and camera speed was set at 16k frames per second. Because the glass tubes were exposed to the ambient air, there was certain level of heating to the glass tubes due to external natural convection. However, since the magnitude is so small, the effect of external natural convection was believed to be too small to enable nucleate boiling. Thus there shall be no bubble nucleation occuring in the glass tube section.

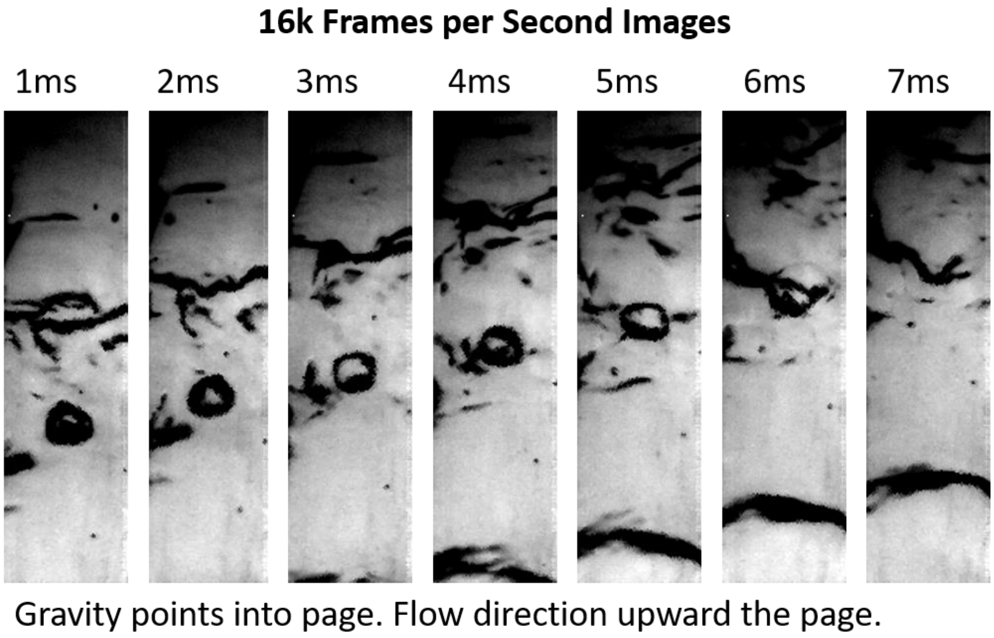

Figure 33 High speed images for the flow inside the glass tube, with lens pointing towards the ground and normal to the tube.

Images shown in Figure 33 were shot with a very short focal length and small distance from the object. The "shutter" speed was sest to 16k frames per second, which allowed extremely fast moving bubbles (typically very small in size) to be captured in the image. The time interval between the images shown in Figure 33 is 10^{-3} s. It was noticable that there was a large bubble in the center of the image and several little bubbles scattered around. The large bubble in the center and the little bubbles at the lower right corner appeared to be moving straight throught the tube with a constant velocity, as the bubble displacement observed between images were roughly equal.

There were also several small bubbles that initially can be found in the first several images but disappeared in the latter images. They were believed to have merged into the larger bubble or bursted in the liquid flow. It was noticable that some bubble-like objects that appeared to be the same size may move at significantly different velocities, which indicated that the velocity distribution in the two-phase phase flow was quite uneven. And it is possible that some of the observed objects were liquid droplets entrained in the vapor flow, which in nature posses larger velocity than the bubbles found in the liquid flow. These high speed images can be used to estimate the liquid and vapor velocities.

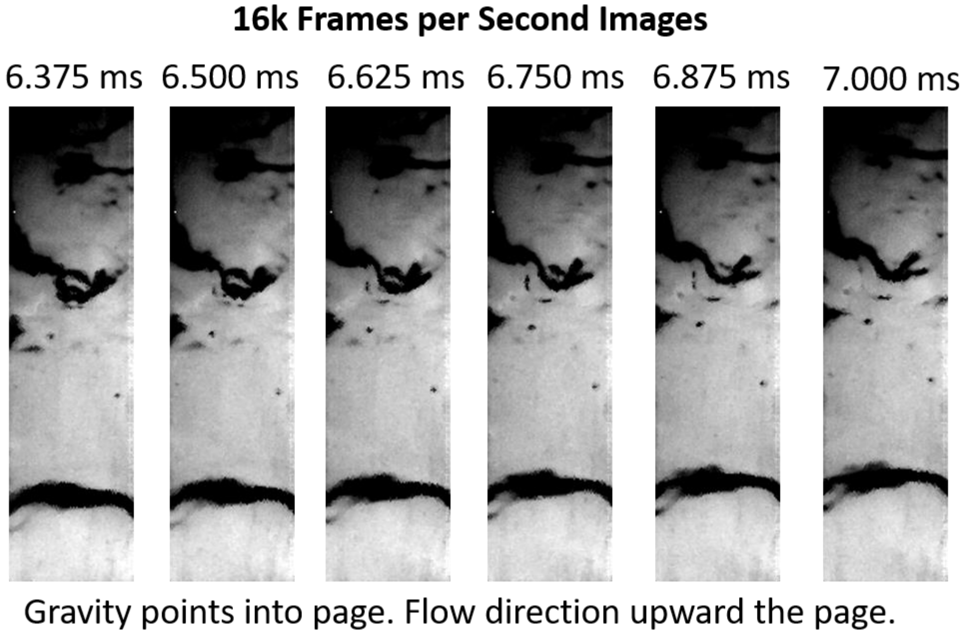

Figure 34 High speed images for the flow inside the glass tube, with lens pointing towards the ground and normal to the tube.

It shall be noticed that the large bubble in the center of the image sight disappeared between 6 ms to 7 ms. The images between this time interval were shown in Figure 34. Based on the images, it was possible that the bubble emerged to the liquid-vapor interface and bursted. It was noted that the little bubble in the lower right corner of the image sight barely moved during this period of time form 6.375 ms to 7 ms, which indicated that the burst of the bubble occurred in a very short period of time.

When it comes to the process of flow regime identification, the drawback of the top-down camera position starts to show, mainly due to the difficulty in locating the vapor-liquid interface, which is critical to the identification of flow regime. Thus, another approach was taken, which was to shoot images from the side of the tube on the same horinzontal plane. Images shown below (see Figure 35) were captured from the side of the 1st glass tube. Each image was labeled with the mass flux, vapor quality at the inlet and the temperature been tested. It was noted that the images taken at 1k fps were more blurry than those taken at 16k fps. This is because an increase in the exposure time increased the distance of travel of objects and thus producing traces instead of sharp edges. Nevertheless, the image quality was sufficient for flow regime identification. In image (1), with a mass flux of 100 kg/m^2-s, vapor quality slightly higher than 0.1 since the first glass tube was close to the inlet, the flow regime was stratified wavy. In image (2), with a mass flux of 150 kg/m^2-s, vapor quality slightly higher than 0.1, the flow regime was between stratified wavy and slug. From images (3) to (5), with a mass flux of 200 kg/m^2-s, vapor quality from 0.1 to 0.5, the flow regime underwent a transition from slug to annular flow. It shall be noted that these flow regime observations agreed well with the flow regime map developed by Thome et. al [49] in 1998.

As the solenoid valves open and close alternately, based on the pressure drop profile, it is evident that the flow velocity profile and vapor quality profile in pulsating flow tests evolves with time. For valve-on time when the mass flux is the high, the flow regime evolves into forms including: stratified wavy (SW), stratified/slug flow (SW/Slug), slug/intermittent flow (Slug/I), annular flow (A). During valve-off time, due to the reduced mass flux, the flow regimes are most dominated by the stratified flow (S) and dry-out flow (D).

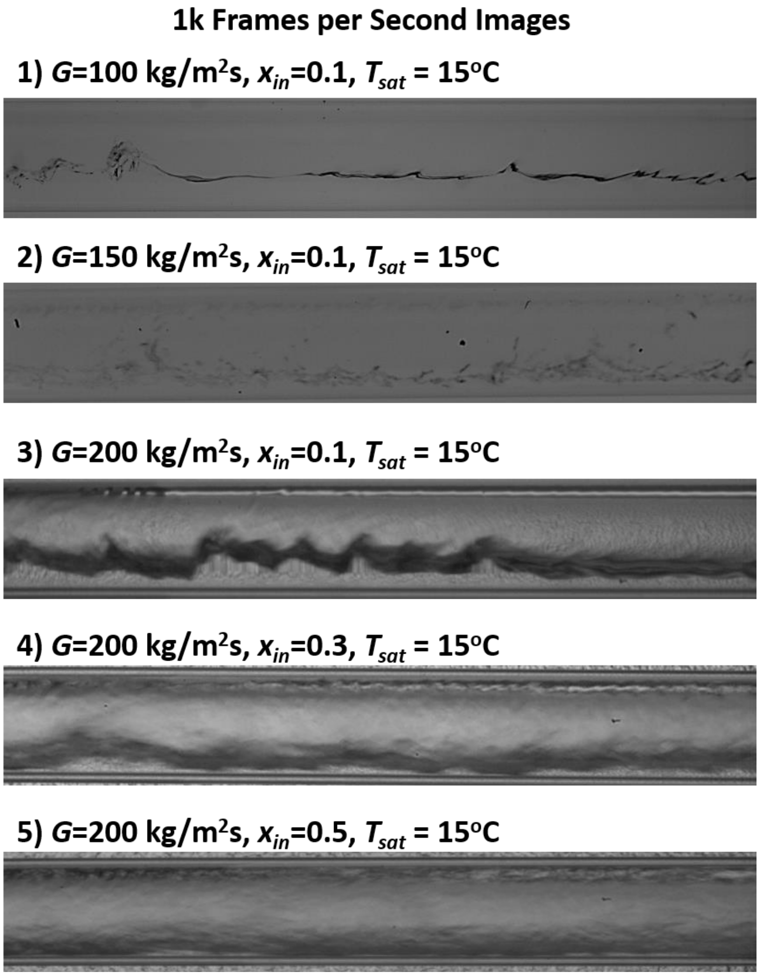

Figure 35 High speed images for the flow inside the glass tube, with lens pointing parallel to the ground and normal to the tube.

High speed photos were taken for the test conditions shown in Table 4. The fraction of each flow regime identified were calculated. The fraction of each flow regime is plotted on the primary *y*-axis against the pulsation period on the *x*-axis in Figure 36 and Figure 37. The secondary *y*-axis on the same graph shows the heat transfer enhancement ratio for each pulsation period which is plotted in dots. In Figure 36(a), data for G=100kg/m^{2}s, inlet and outlet vapor quality=0.1 and 0.8 was plotted. It was shown that the heat transfer enhancement ratio decreases with the increase of the fraction of dry-out flow. When the dry-out flow fraction exceeds 40%, the enhancement ratio falls below one, which means the pulsating flow heat transfer coefficient is lower than that of the continuous flow. The similar trend is also found in Figure 38(b), where G=150kg/m^{2}s, inlet vapor quality=0.4 and outlet vapor quality=0.8. The enhancement ratio also falls below one when the fraction of the dry-out flow goes over 40%.

Table 4 Test conditions that had the flow regime visualization results.

G (kg/m^{2}s)	**Vapor Quality**	**Flow pulsation condition**
100	0.1-0.8	Continuous, Pulsating: period = 2, 12, 24s
150	0.4-0.8	
200	0.1-0.8	
200	0.4-0.8	

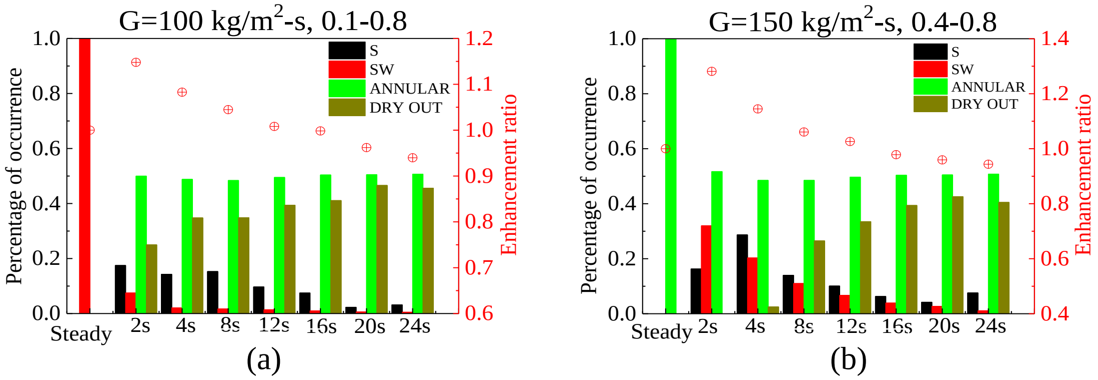

Figure 36 Statistical data for flow regime and heat transfer enhancement ratio (a)G=100kg/m^{2}s, x=0.1-0.8; (b)G=150kg/m^{2}s, x=0.4-0.8

In Figure 37, some data with G=200kg/m^{2}s is plotted in the same style. It was shown that the heat transfer enhancement also decreases as the fraction of the dry-out flow increases. However, while comparing data from Figure 36(b) and Figure 37(b), where the vapor quality ranges are the same but different mass fluxes, it was noted that the heat transfer enhancement ratio for a higher mass flux (see Figure 37(b)) is consistently lower than that of a lower mass flux (see Figure 36(b)) for all pulsation periods for about 10%, while the fractions for the dry-out flow does not differ significantly. Since the nucleate boiling contribution to the heat transfer is expected to be lower in a flow with higher velocity due to the suppression of nucleate boiling [50], it is an indirect evidence that the enhancement in heat transfer with pulsating flow is highly dependent on the strength of the nucleate boiling heat transfer.

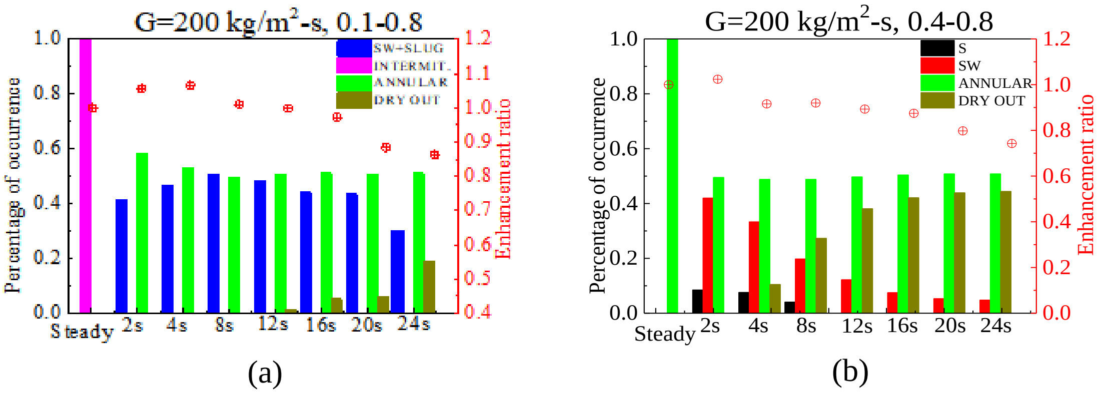

Figure 37 Statistical data for flow regime and heat transfer enhancement ratio (a)G=200kg/m^{2}s, x=0.1-0.8; (b)G=200kg/m^{2}s, x=0.4-0.8

The enhancement ratio of the heat transfer coefficient was then plotted against the fraction of flow regimes in Figure 38, where each graph panel titled with the name of the flow regime and the *x*-axis representing the fraction of the flow regime at a scale from 0-1. In Figure 38, different test conditions with the same equivalent mass flux used the same marker. It was noted that the enhancement ratio in heat transfer coefficient decreases with a greater fraction of stratified and wavy flow for *G*=200 kg/m^{2}s. However, the reasoning behind the correlation between the SW flow and the heat transfer remains unclear.

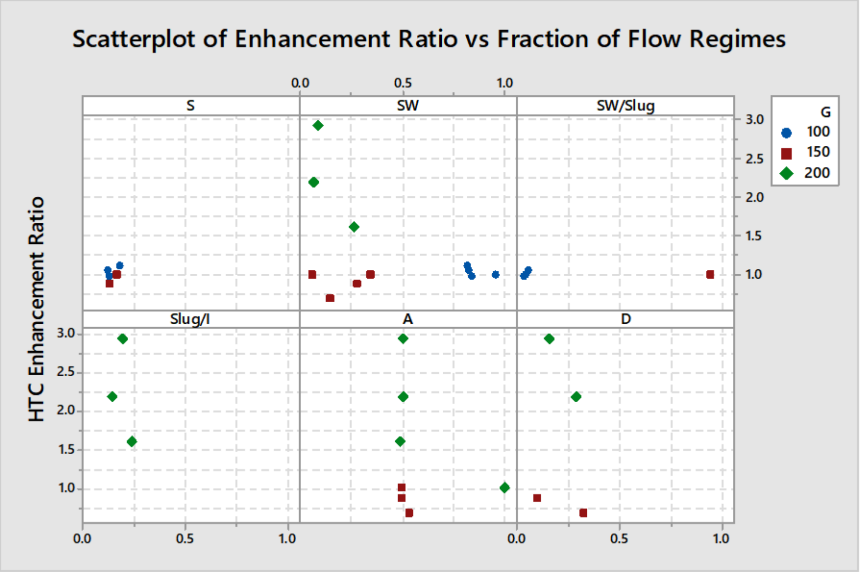

Figure 38 Enhancement ratio versus flow regime statistics for test conditions in Table 4.

4 Modeling of Pulsing Flow

A temporal pressure drop model is developed to predict pressure drop during pulsating flow. A time-averaged heat transfer model of pulsating flow is also built based on the quasi-steady state assumption using the temporal pressure drop model combined with the existing steady heat transfer model. The model consists of three parts, part one: a correlation predicting the temporal pressure drop profile; part two: a scaling method predicting the temporal mass flux profile using the pressure drop profile; part-three: a quasi-steady model combined with empirical steady flow correlations calculating the overall heat transfer coefficient of the heat exchanger based on the predicted mass flux profile made in part two. Each part is described in detail in the following sections.

4.1 Correlation for the Temporal Pressure Drop Profile

This correlation was designed two predict the pulsating flow pressure drop profile in time-domain using average value of the operating parameters. An asymptotic model was built to predict the pressure drop behavior during both valve-on time and off-time (see equation (8)).

$$\Delta p(t) = \theta_1 - \theta_2 e^{-\theta_3 t} \tag{8}$$

where $\Delta p(t)$ = pressure drop [Pa] of the test section varying with time. It was found that when the parameters in equation (8) are set to the following values, the function provides the best fit to the experimental data for valve on-time:

$$\theta_{1-on} = \Delta p_{\max} \tag{9}$$

$$\theta_{2-on} = \Delta p_{\max} - \Delta p_{\min} \tag{10}$$

And for valve off time:

$$\theta_{1-off} = \Delta p_{\min} \tag{11}$$

$$\theta_{2-off} = \Delta p_{\min} - \Delta p_{\max} \tag{12}$$

where Δp_{max} and Δp_{min} are the maximum and minimum pressure drop in a pulsation period, respectively. Predictions of the value for these two parameters were made using a set of correlations developed by the author (see equation (13) and (14)), which are based on the time averaged operating conditions:

$$\Delta p_{\max} / \Delta p_{baseline} = \left(Re_{le}^{-0.38} Bo^{-0.46}\right)^{\tau_{le}^{0.13}} \tag{13}$$

$$\Delta p_{\min} / \Delta p_{baseline} = \left(Re_{le}^{1.5} Bo^{1.8}\right)^{\tau_{le}^{0.2}} \tag{14}$$

where $\Delta p_{baseline}$ = pressure drop of the test section in continuous flow [Pa], which can be predicted using steady state two-phase flow pressure drop correlations from many widely acknowledged work [51-53]. The other parameters used in equation (13) and (14) are defined below:

$\tau_{le} = \frac{\tau}{T_{le}}$ = dimensionless pulsation period parameter

τ= pulsation period [s]

$T_{le} = L\rho_l/G$

ρ_l = density of liquid phase refrigerant [kg/m^3]

L = total tube length in the test section [m]

G = time-averaged mass flux [kg/(m2-s)]

D = inner diameter of the tube [m]

$Bo = q''/Gh_{lv}$ = Boiling Number

q'' = time-averaged heat flux applied to the test section [W/m^2]

h_{lv} = latent heat of refrigerant [kJ/kg]

The accuracy of the predictions for Δp_{max} and Δp_{min} are validated using experimental data. The predicted results for Δp_{max} and Δp_{min} were plotted against the experimental data in Figure 39 and Figure 40. The deviation between the pressure drop correlation and data were summarized in the histogram charts in Figure 41 and Figure 42. In total, 82.5% of the predictions fall in a deviation interval of ±30%.

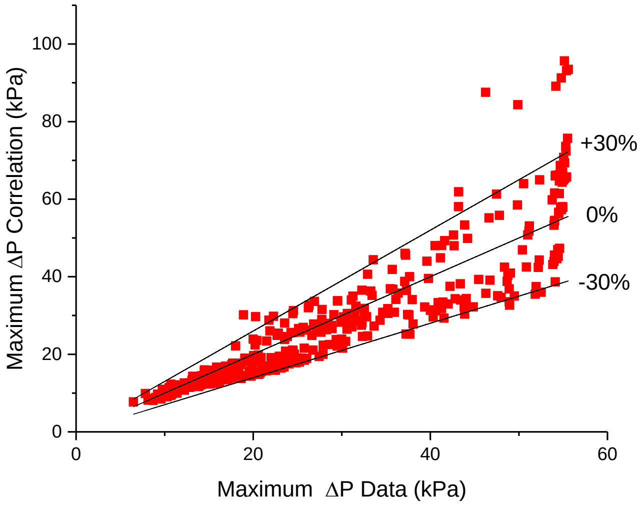

Figure 39 Comparison between the maximum Δp correlations and the experimental data.

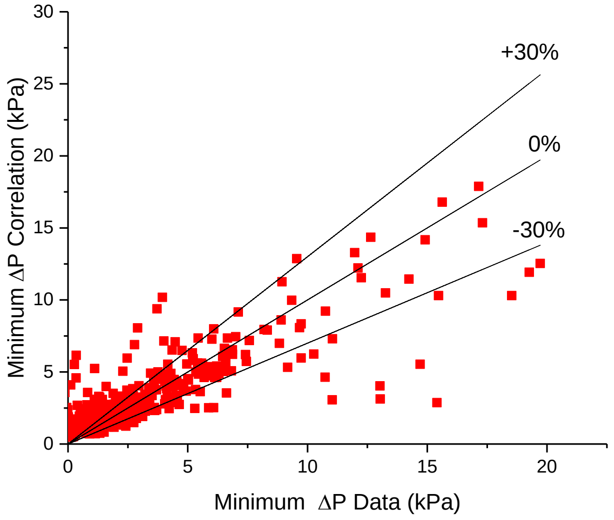

Figure 40 Comparison between the maximum Δp correlations and the experimental data.

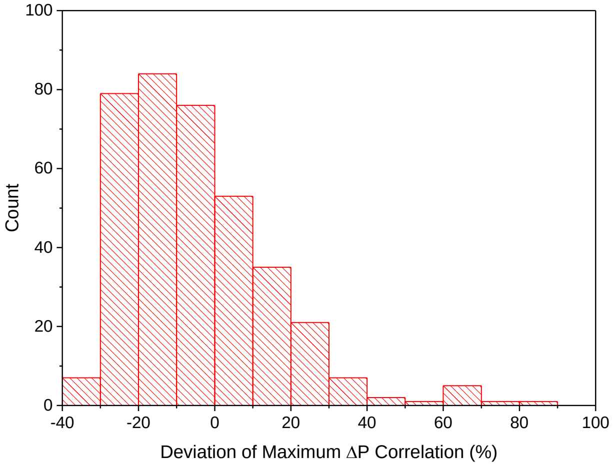

Figure 41 Histogram of the deviation between the maximum Δp correlation and data.

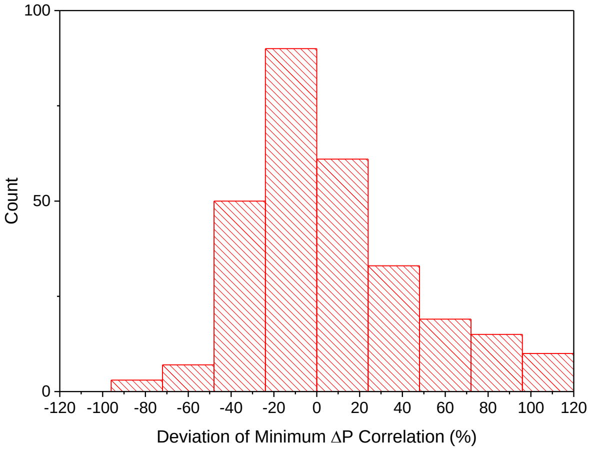

Figure 42 Histogram of the deviation between the minimum Δp correlation and data.

Combining equation (9) to (14), predictions for the parameters θ_1, θ_2 in equation (8) can be calculated. Another empirical correlation for the parameter θ_3 was introduced to bring a close-form expression for equation (8):

$$\text{Valve on-time: } \theta_{3\_on} = 0.03 Re_{le}^{0.42} Bo^{0.11} \tau_{le}^{-0.7} \tag{15}$$

$$\text{Valve off-time: } \theta_{3\_off} = 1.25\times10^{4} Re_{le}^{-0.86} Bo^{0.19} \tau_{le}^{-0.26} \tag{16}$$

Combing equation (9) to (16), the final closed form of equation (8) can be written as:

$$t < \frac{\tau}{2} : \Delta P(t) = \theta_{1\text{-}on} - \theta_{2\text{-}on} \exp\left[-\theta_{3\text{-}on} t\right] \tag{17}$$

$$t \geq \frac{\tau}{2} : \Delta P(t) = \theta_{1-off} - \theta_{2-off} \ \exp\left[-\theta_{3-off} \left(t - \tau / 2\right)\right] \tag{18}$$

The accuracy of the prediction provided by equation (8) is validated using experimental data. The comparison between the predicted and measured temporal variation in the pressure drop was plotted in Figure 43 to Figure 45, where the yellow curves represent experimental data and the blue curves represent prediction made by the correlation:

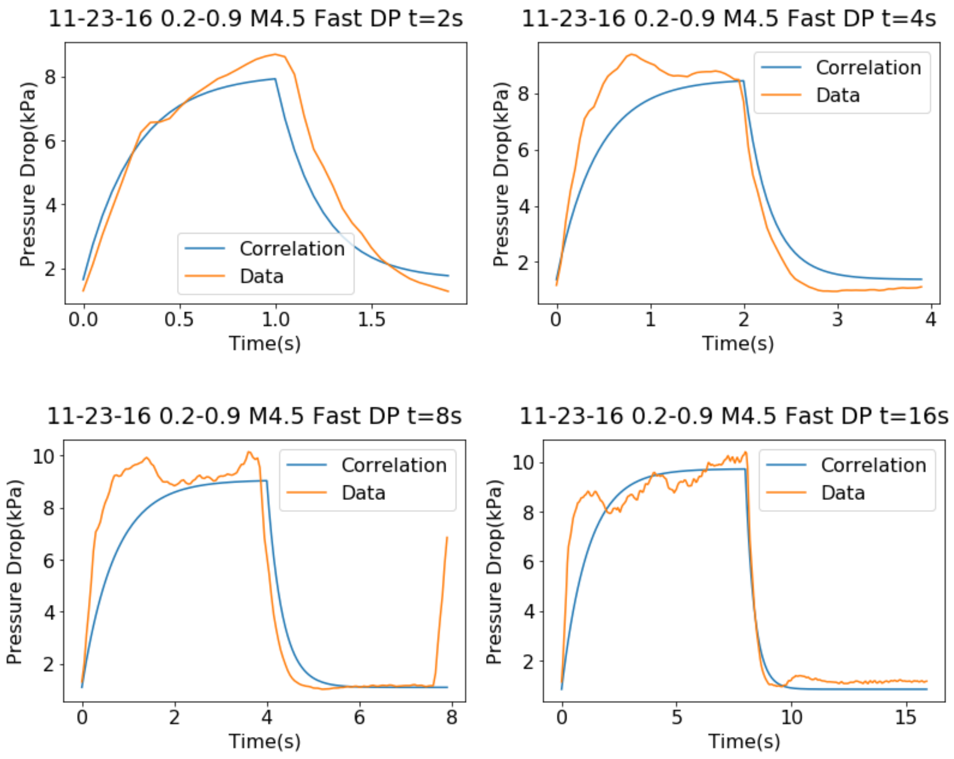

Figure 43 The temporal pressure drop variation for G=75 kg/m2-s, x=0.2 to 0.9, Pulsation Period=2 to 20 s

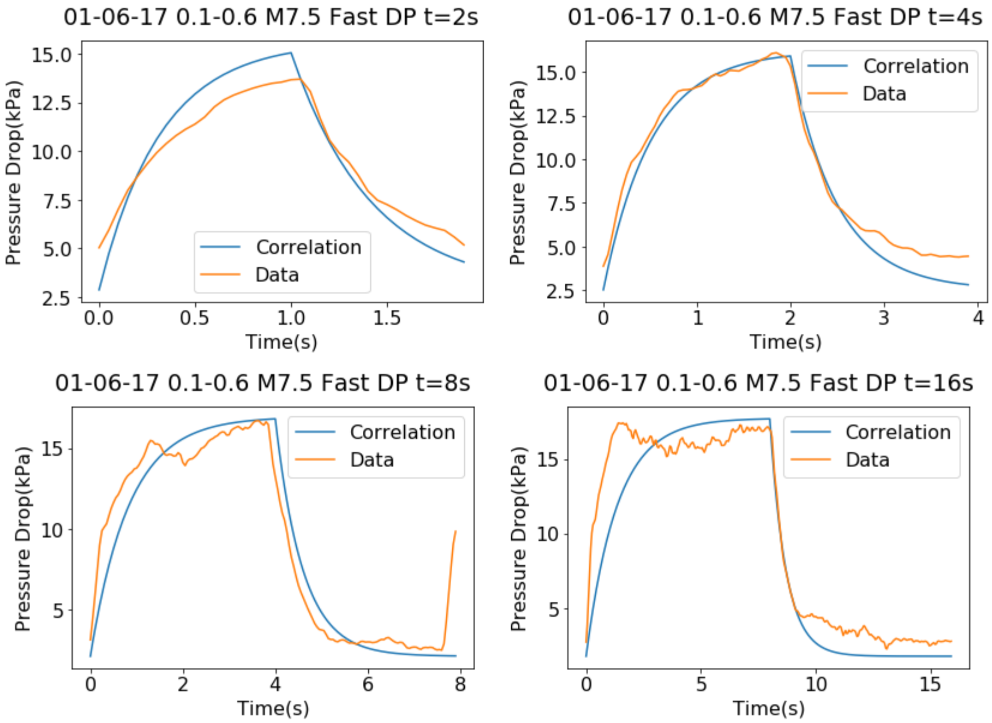

Figure 44 The temporal pressure drop variation for G=125 kg/m2-s, x=0.3 to 0.7, Pulsation Period=2 to 20s

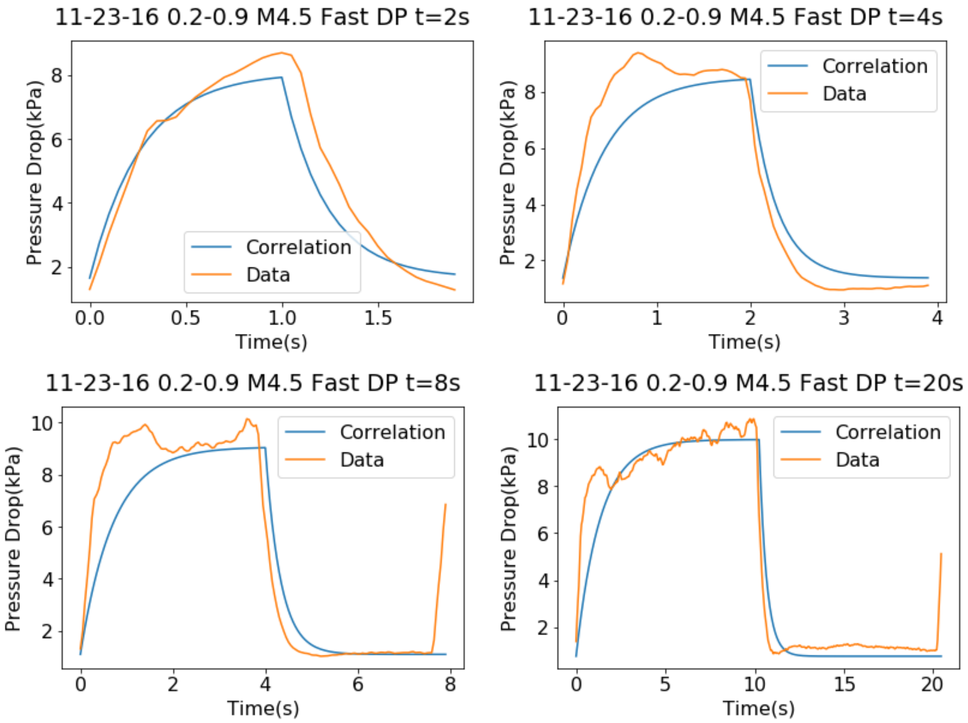

Figure 45 The temporal pressure drop variation for G=175 kg/m2-s, x=0.1 to 0.8, Pulsation Period=2 to 20 s

4.2 Scaling Method Calculating the Mass Flux Profile based on the Pressure Drop

The temporal mass flux is a necessary parameter for the calculation of the temporal heat transfer coefficient. However, due to the limitation in two-phase flow rate measurement techniques, the temporal mass flux in two-phase flow cannot be measured directly. To solve this problem, the author proposed a method using scaling technique to approximate the temporal mass flux profile using the temporal pressure drop profile. This method was based on the momentum balance equation of two phase flow:

$$-\left(\frac{dp}{dz}\right) = -\left(\frac{dp}{dz}\right)_{fr} + [(1-\alpha)\cdot\rho_l + \alpha\cdot\rho_v]\cdot g\cdot sin\Omega + \frac{d}{dz}[\frac{G^2\cdot x^2}{\rho_v\cdot\alpha} + \frac{G^2\cdot(1-x)^2}{\rho_l\cdot(1-\alpha)}] \qquad (19)$$

where $\alpha =$ void fraction of the refrigerant flow

$\Omega =$ inclination angle of the tube

$x =$ vapor quality of the refrigerant

By using the two-phase multiplier Φ_l, the frictional pressure drop term can be written as:

$$-\left(\frac{dp}{dz}\right)_{fr} = -\Phi_l^2\left(\frac{dp}{dz}\right)_l \tag{20}$$

$$\left(\frac{dp}{dz}\right)_l = \frac{f_l G^2 (1-x)^2}{\rho_l r_o} \tag{21}$$

The Lockhart and Martinelli correlation for the two-phase multiplier Φ_l can be written in the relations below:

$$\Phi_l^2 = 1 + \frac{C}{X} + \frac{1}{X^2}$$

$$X = \left(\frac{1-x}{x}\right)^{0.875}$$

$$C = 5\ to\ 20$$

Through leading term approximation, the multiplier can be expressed in the following relation:

$$\Phi_l^2 = 1 + C\left(\frac{1-x}{x}\right)^{-0.875} + \left(\frac{1-x}{x}\right)^{-1.75} \tag{22}$$

In the similar fashion, the pressure gradient of liquid flowing alone in the tube can be written in the relation below:

$$\left(\frac{dp}{dz}\right)_l \sim G^2 \cdot (1-x)^2 \cdot f_l \tag{23}$$

where the friction factor f_l:

$$f_l \sim [G \cdot (1-x)]^{-0.25} \tag{24}$$

Combing equations (20) to (24) the frictional pressure drop term in equation (19) can be written in the relation below:

$$\Phi_l^2 \cdot \left(\frac{dp}{dz}\right)_l \sim G^{1.75} \cdot (1-x)^{1.75} \cdot [\left(\frac{1-x}{x}\right)^{-0.875} + \left(\frac{1-x}{x}\right)^{-1.75}] \tag{25}$$

Since the tubes in the test section was horizontal, the gravitational term in equation (19) became zero:

$$-\left(\frac{dp}{dz}\right) \sim \Phi_l^2 \left(\frac{dp}{dz}\right)_l + \frac{d}{dz}[\frac{G^2x^2}{\rho_v \cdot \alpha} + \frac{G^2 \cdot (1-x)^2}{\rho_l \cdot (1-\alpha)}]$$

Integration gives:

$$\Delta p \sim \int \Phi_l^2 \left(\frac{dp}{dz}\right)_l dz + \int d\left(\frac{G^2x^2}{\rho_v \cdot \alpha} + \frac{G^2 \cdot (1-x)^2}{\rho_l \cdot (1-\alpha)}\right) \tag{26}$$

Combining equation (25) and (26) yields:

$$\Delta p \sim G^{1.75} \cdot \int \left[\left(\frac{1-x}{x}\right)^{0.875} + x^{1.75}\right] dz + \frac{G^2x^2}{\rho_v \cdot a} + \frac{G^2 \cdot (1-x)^2}{\rho_l \cdot (1-\alpha)} \tag{27}$$

The function $f = \left(\frac{1-x}{x}\right)^{0.875} + x^{1.75}$ can be approximated using the exponential function

$$f^* = 0.764 * x^{-0.925}$$

Equation (27) can be further simplified:

$$\Delta p \sim G^{1.75} \cdot 10.19 \cdot x^{0.075} + \frac{G^2x^2}{\rho_v \cdot a} + \frac{G^2 \cdot (1-x)^2}{\rho_l \cdot (1-\alpha)}$$

Where the term $x^{0.075}$ is approximately equal to one, the equation can be simplified as

$$\Delta p \sim G^{1.75} \cdot 10.19 + \frac{G^2 x^2}{\rho_v \cdot a} + \frac{G^2 \cdot (1-x)^2}{\rho_l \cdot (1-\alpha)} \tag{28}$$

Since $\rho_v \gg 1$ and $\rho_l \gg 1$, the last two terms in equation (28) can be neglected. The final relation between the instantaneous pressure drop ΔP and mass flux G can be reached

$$\Delta p \sim G^{1.75} \tag{29}$$

Which has the equivalent expression

$$\Delta p(t) = C_1 G(t)^{1.75} \tag{30}$$

Where C_1 is a constant independent of time, which can be determined using the mass conservation equation:

$$\int_{t_i}^{t_f} G(t)\, dt = \bar{G} \cdot (t_f - t_i) \tag{31}$$

where $\bar{G}$ = time-averaged mass flux of the refrigerant flow [kg/m^2-s]

t_i and t_f = the start and final time point in one complete pulsation period [s]

Combining equation (30) and (31) yields:

$$\int_{t_i}^{t_f} \left(\frac{\Delta p(t)}{C_1}\right)^{-1.75} dt = \bar{G} \cdot (t_f - t_i) \tag{32}$$

Through a numerical integration of the predicted temporal pressure drop profile $\Delta p(t)$ (see Section 4.1) over a full period, the constant C_1 can be determined for any given flow parameters. Substituting C_1 into equation (30), the temporal mass flux value can be calculated based on the temporal pressure drop, which can be predicted using the proposed correlations in Section 4.1.

4.3 Quasi-steady State Model Calculating the Time-averaged Heat Transfer

The modeling procedure for pulsating flow is outlined in Figure 46. It shall be noted that an estimated average heat flux to the pulsating flow is needed to obtain the mass flux profile. Nevertheless, the local heat flux must be solved iteratively to obtain the local heat transfer coefficient, which was calculated using the Wojtan et al. correlation [47] and the local pressure drop, which takes the decrease in the saturation temperature along the tube into count, was also calculated using several widely accepted correlations [51, 52]. The local heat transfer coefficient was then integrated along the tube direction and time domain to obtain the time-averaged overall heat transfer coefficient.

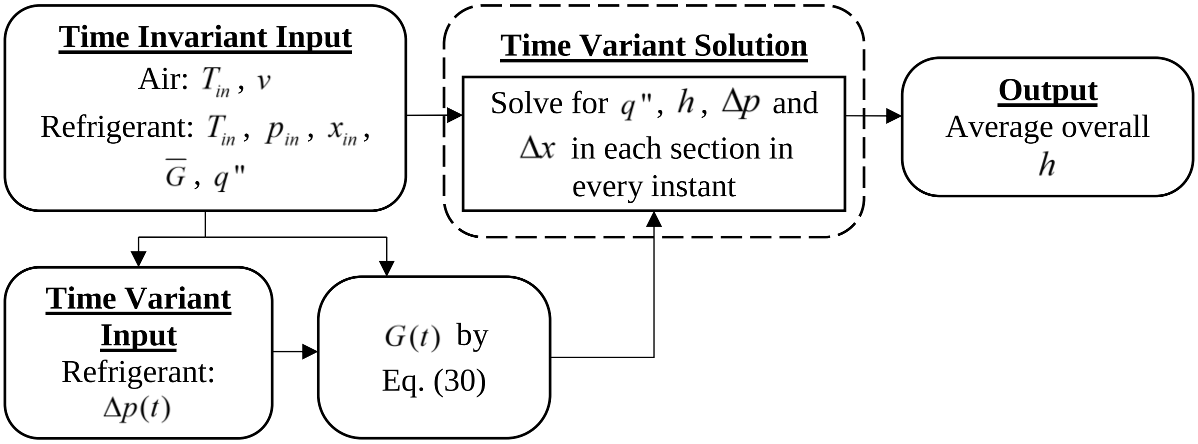

Figure 46 Outline for the model of pulsating flow heat transfer

The following assumptions were made in this model:

1. The mass flow rate of air at any point over the heat exchanger was constant. The validity of this assumption was supplemented with air flow velocity profiling data shown in appendix A.
2. Radiation heat transfer neglected.
3. Conduction heat transfer along the tube axis is neglected.

4. The inlet vapor quality of the refrigerant flow is constant throughout the entire pulsation period.
5. Quasi-steady steady assumption.
6. The mass flux at any instant is spatially uniform along the test section.

The deviation between the heat transfer modeling results and experimental data were plotted in the following histogram, where the percentage of number of points in every 10 percent mean deviation were plotted in Figure 47. It was noted that over 80 percent of all data points fall within ±20%, while all data point fall within the ±40% range.

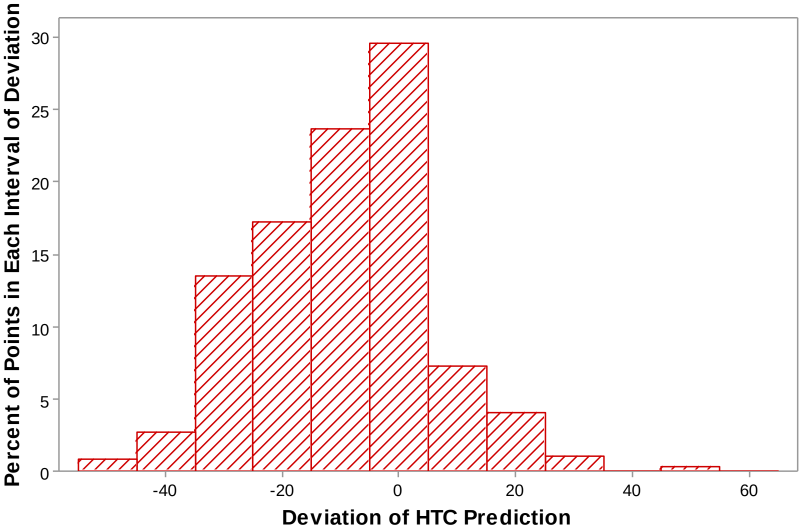

Figure 47 Deviation chart of the heat transfer coefficient modeling results

Since in pulsating flow, the mass flow rate during the valve off-time may drop down to a very small value, which may cause the flow to fall into the laminar flow regime, the accuracy of the current modeling approach using turbulent two-phase flow steady state correlations may raise concerns in the accuracy for these flow conditions. Thus, the modeling deviation data were then separated by the approximate mean mass flux and plotted in Figure 48 to demonstrate the modeling-data agreement in both low and high mass flux flow conditions. The statistics of the same deviation data was summarized in Table 5**.**

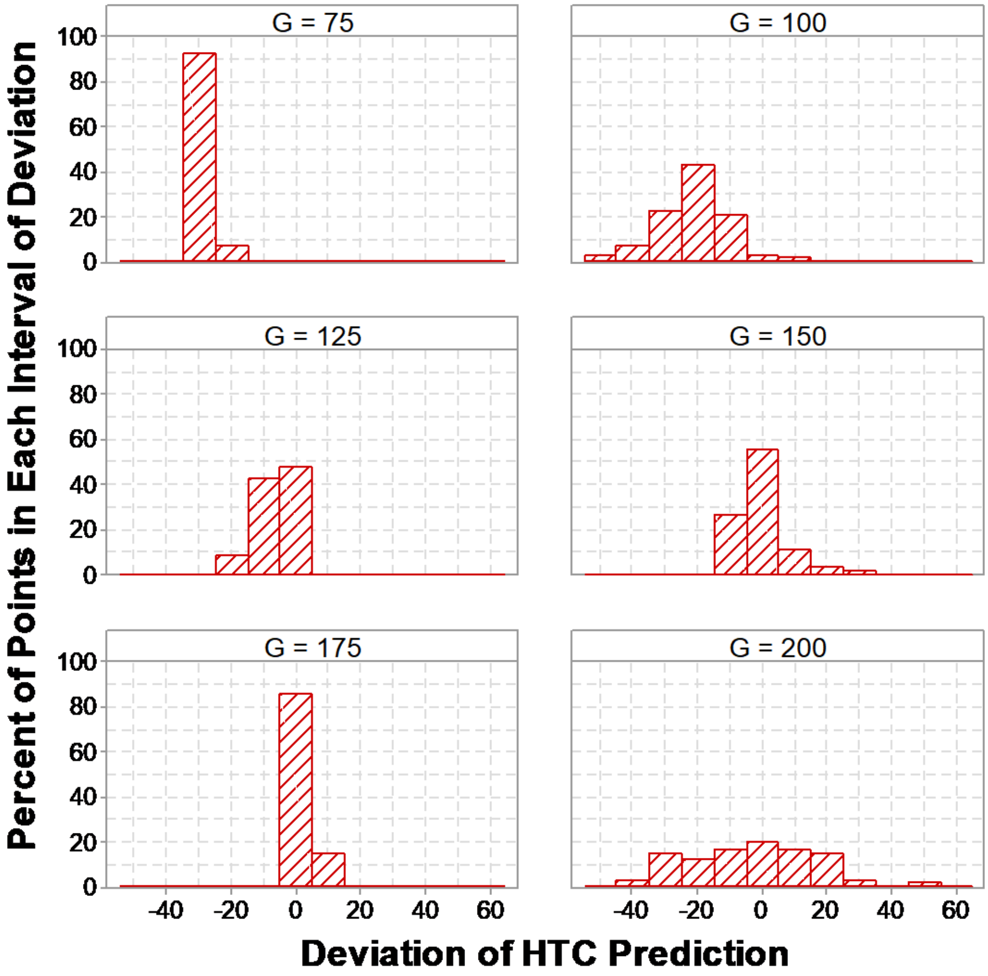

Figure 48 Deviation between the predicted heat transfer coefficient and experimental data. The results are separated by mass flux.

Table 5 Summary of the deviation of predicted HTC for different mass flux.

Mass Flux (kg/m²s)	**# of data points**	**Predicted HTC Range (W/m²s)**	**Exp. HTC Range (W/m²s)**	**Deviation Range (%)**
75	14	752 - 853	983 - 1124	-25 to -23
100	102	696 - 1139	869 - 1346	-36 to +8.4
125	56	860 - 1554	1067 – 1584	-11 to +1
150	100	938 - 1987	879 - 1906	-10 to +21
175	7	1849 - 2179	1846 - 2230	-3 to +1
200	56	727 - 2308	541 - 2443	-19 to +34

5 Conclusions

Saturated liquid-vapor two-phase flow subjected to flow pulsation during evaporation and boiling has been studied both by experiment and modeling in this work. Flow with R-134a was tested under heat exchange with ambient air through a plain fin evaporator under different conditions. Effects of air flow rate, refrigerant mass flow rate, inlet vapor quality, and pulsating period on heat transfer coefficient and pressure drop during pulsating flow has been addressed and compared with continuous flow. Liquid-vapor two-phase flow was recorded by a high-speed camera and flow regimes has also been statically analyzed according to the captured images. Modeling of pulsating flow was developed based on the quasi-steady assumption. Temporal pressure drop is related to the period, mass and heat flux through a semi-empirical correlation. The dimensionless scale analysis was conducted to predict temporal mass flux using the temporal pressure drop. Heat transfer coefficient was then calculated using the temporal mass flux combined with existing steady flow models based on the quasi-steady state assumption.

The result of current study shows that:

1) The enhancement in heat transfer coefficient of pulsating flow varies from -33% to +130% comparing to continuous flow at the same equivalent mass flux depending on different conditions;

2) The pulsation period is a major factor and plays a significant role to the heat transfer enhancement;

3) The difference in pressure drop of pulsating flow compared to that of continuous flow varies from -17% to +52%.

4) It was also found that for pulsating flow, a lower vapor quality at the inlet generally produced a higher heat transfer coefficient and a lower pressure drop at the same time;
5) This model provides an easy to use approach to predict pulsating flow heat transfer and pressure drop for the first time. It gives a mean deviation of -11.34%% and a standard deviation of 14.69% compared to experimental data.

.

References

1. Ilic, S., P. Hrnjak, and C. Bullard, *Experimental comparison of continuous vs. pulsed flow modulation in vapor compression systems*. 2002.
2. Uribe, T., C. Bullard, and P. Hrnjak, *Designing and optimizing systems for compressor rapid cycling*. 2003, Air Conditioning and Refrigeration Center. College of Engineering. University of Illinois at Urbana-Champaign.
3. Ilic, S., C. Bullard, and P. Hrnjak, *Effect of shorter compressor on/off cycle times on a/c system performance*. 2001, Air Conditioning and Refrigeration Center. College of Engineering. University of Illinois at Urbana-Champaign.
4. Brooks, M., et al. *Pulse-driven refrigeration: Progresses and challenges*. in *International Energy Conversion Engineering Conference (IECEC), AIAA, Denver, CO*. 2009.
5. Du Clou, S., et al. *Pulsed Ejector Cooling System*. in *10th International Energy Conversion Engineering Conference (IECEC)*. 2012.
6. Weislogel, M.M. and M.A. Bacich. *A high performance semi-passive cooling system: The Pulse Thermal Loop*. 2004.
7. Kuendig, A. and H. Schoenfeld. *Helium refrigerator design for pulsed heat load in tokamaks*. in *AIP Conference Proceedings*. 2006. AIP.
8. Dutta, R., P. Ghosh, and K. Chowdhury, *Mitigation of effects of pulsed heat loads in helium refrigerators for fusion devices using supercritical helium storage.* IEEE transactions on applied superconductivity, 2012. **22**(6): p. 4203712-4203712.
9. Hoa, C., et al., *Heat load estimator for smoothing pulsed heat loads on supercritical helium loops.* Physics Procedia, 2015. **67**: p. 1147-1152.

10. Pendyala, R., S. Jayanti, and A. Balakrishnan, *Convective heat transfer in single-phase flow in a vertical tube subjected to axial low frequency oscillations.* Heat and Mass Transfer, 2008. **44**(7): p. 857-864.

11. Outtagarts, A., P. Haberschill, and M. Lallemand, *The transient response of an evaporator fed through an electronic expansion valve.* International Journal of Energy Research, 1997. **21**(9): p. 793-807.

12. Tamainot-Telto, Z., et al., *Behaviour of a thermostatic expansion valve in non-steady state for a refrigerating machine.* International Journal of Refrigeration, 1996. **19**(2): p. 124-131.

13. Tian, C., et al., *Experimental investigation into hunting of an automotive air-conditioning system with variable displacement compressor and thermal expansion valve.* Proceedings of experimental methods and measuring techniques in refrigeration, Liège, Belgium, 2000.

14. Lazzarin, R. and M. Noro, *Experimental comparison of electronic and thermostatic expansion valves performances in an air conditioning plant.* International journal of refrigeration, 2008. **31**(1): p. 113-118.

15. Tian, C., et al., *Instability of automotive air conditioning system with a variable displacement compressor. Part 2. Numerical simulation.* International journal of refrigeration, 2005. **28**(7): p. 1111-1123.

16. Tuo, H. and P. Hrnjak, *Periodical reverse flow and boiling fluctuations in a microchannel evaporator of an air-conditioning system.* International journal of refrigeration, 2013. **36**(4): p. 1263-1275.

17. Tuo, H. and P. Hrnjak, *Visualization and measurement of periodic reverse flow and boiling fluctuations in a microchannel evaporator of an air-conditioning system.* International Journal of Heat and Mass Transfer, 2014. **71**: p. 639-652.

18. Chang, K. and C. Pan, *Two-phase flow instability for boiling in a microchannel heat sink.* International Journal of Heat and Mass Transfer, 2007. **50**(11): p. 2078-2088.

19. Womersley, J.R., *XXIV. Oscillatory motion of a viscous liquid in a thin-walled elastic tube—I: the linear approximation for long waves.* The London, Edinburgh, and Dublin Philosophical Magazine and Journal of Science, 1955. **46**(373): p. 199-221.

20. Uchida, S., *The pulsating viscous flow superposed on the steady laminar motion of incompressible fluid in a circular pipe.* Zeitschrift für Angewandte Mathematik und Physik (ZAMP), 1956. **7**(5): p. 403-422.

21. Siegel, R. and M. Perlmutter, *Heat transfer for pulsating laminar duct flow.* ASME J. Heat Transfer, 1962. **84**(2): p. 111-123.

22. Baird, M., et al., *Heat transfer in pulsed turbulent flow.* Chemical Engineering Science, 1966. **21**(2): p. 197-199.

23. Keil, R. and M. Baird, *Enhancement of heat transfer by flow pulsation.* Industrial & Engineering Chemistry Process Design and Development, 1971. **10**(4): p. 473-478.

24. Krishnan, K. and V. Sastri, *Pulsating flows in heat exchangers—an experimental study.* Heat and Mass Transfer, 1982. **16**(3): p. 169-173.

25. Kim, S.Y., B.H. Kang, and J.M. Hyun, *Heat transfer in the thermally developing region of a pulsating channel flow.* International journal of heat and mass transfer, 1993. **36**(17): p. 4257-4266.

26. Elshafei, E.A.M., et al., *Experimental study of heat transfer in pulsating turbulent flow in a pipe.* International Journal of Heat and Fluid Flow, 2008. **29**(4): p. 1029-1038.

27. Habib, M., et al., *Heat transfer characteristics of pulsated turbulent pipe flow.* Heat and mass transfer, 1999. **34**(5): p. 413-421.

28. Karamercan, O.E. and J.L. Gainer, *The effect of pulsations on heat transfer.* Industrial & Engineering Chemistry Fundamentals, 1979. **18**(1): p. 11-15.

29. Wang, X., K. Tang, and P.S. Hrnjak, *Evaporator performance enhancement by pulsation width modulation (PWM).* Applied Thermal Engineering, 2016. **99**: p. 825-833.

30. Kærn, M.R., et al., *Continuous vs. pulsating flow boiling. Part 1: Experimental comparison and visualization.* 2016.

31. Hessami, M.-A., A. Berryman, and P. Bandopdhayay. *Heat transfer enhancement in an electrically heated horizontal pipe due to flow pulsation*. in *ASME 2003 International Mechanical Engineering Congress and Exposition*. 2003. American Society of Mechanical Engineers.

32. Chen, C., W. Chang, and T. Lin, *Time periodic flow boiling heat transfer of R-134a and associated bubble characteristics in a narrow annular duct due to flow rate oscillation.* International Journal of Heat and Mass Transfer, 2010. **53**(19): p. 3593-3606.

33. Mackley, M. and P. Stonestreet, *Heat transfer and associated energy dissipation for oscillatory flow in baffled tubes.* Chemical Engineering Science, 1995. **50**(14): p. 2211-2224.

34. Persoons, T., et al. *Heat transfer enhancement due to pulsating flow in a microchannel heat sink*. in *Thermal Investigations of ICs and Systems, 2009. THERMINIC 2009. 15th International Workshop on*. 2009. IEEE.

35. Ludlow, J., D. Kirwan, and J. Gainer, *Heat transfer with pulsating flow.* Chemical Engineering Communications, 1980. **7**(4-5): p. 211-218.

36. Jacobi, A.M. and R.P. Lucht, *Time-resolved thermal boundary-layer structure in a pulsatile reversing channel flow*. Urbana, 2001. **51**: p. 61801.

37. Rabadi, N., J. Chow, and H. Simon, *Heat transfer in curved tubes with pulsating flow.* International Journal of Heat and Mass Transfer, 1982. **25**(2): p. 195-203.

38. Sailor, D.J., D.J. Rohli, and Q. Fu, *Effect of variable duty cycle flow pulsations on heat transfer enhancement for an impinging air jet.* International Journal of Heat and Fluid Flow, 1999. **20**(6): p. 574-580.

39. Xu, P., et al., *Turbulent impinging jet heat transfer enhancement due to intermittent pulsation.* International Journal of Thermal Sciences, 2010. **49**(7): p. 1247-1252.

40. Gupta, S.K., R.D. Patel, and R.C. Ackerberg, *Wall Heat Mass-Transfer in Pulsatile Flow.* Chemical Engineering Science, 1982. **37**(12): p. 1727-1739.

41. Pendyala, R., S. Jayanti, and A. Balakrishnan, *Flow and pressure drop fluctuations in a vertical tube subject to low frequency oscillations.* Nuclear Engineering and Design, 2008. **238**(1): p. 178-187.

42. Wang, C., et al., *Experimental study on friction and heat transfer characteristics of pulsating flow in rectangular channel under rolling motion.* Progress in Nuclear Energy, 2014. **71**: p. 73-81.

43. ElSherbini, A., A. Jacobi, and P. Hrnjak, *Experimental investigation of thermal contact resistance in plain-fin-and-tube evaporators with collarless fins.* International Journal of Refrigeration, 2003. **26**(5): p. 527-536.

44. Hong, K.T. and R.L. Webb, *Calculation of fin efficiency for wet and dry fins.* HVAC&R Research, 1996. **2**(1): p. 27-41.

45. Youn, B. and R. Webb, *Air-side heat transfer and friction correlations for plain fin-and-tube heat exchangers with staggered tube arrangements.* 1999.

46. Wojtan, L., T. Ursenbacher, and J.R. Thome, *Investigation of flow boiling in horizontal tubes: Part I—A new diabatic two-phase flow pattern map.* International Journal of Heat and Mass Transfer, 2005. **48**(14): p. 2955-2969.

47. Wojtan, L., T. Ursenbacher, and J.R. Thome, *Investigation of flow boiling in horizontal tubes: Part II—Development of a new heat transfer model for stratified-wavy, dryout and mist flow regimes.* International Journal of Heat and Mass Transfer, 2005. **48**(14): p. 2970-2985.

48. Kattan, N., J.R. Thome, and D. Favrat, *Flow boiling in horizontal tubes: Part 2 - New heat transfer data for five refrigerants.* Journal of Heat Transfer-Transactions of the Asme, 1998. **120**(1): p. 148-155.

49. Kattan, N., J.R. Thome, and D. Favrat, *Flow boiling in horizontal tubes: part 3—development of a new heat transfer model based on flow pattern.* Journal of Heat Transfer, 1998. **120**(1): p. 156-165.

50. Chen, J.C., *Correlation for boiling heat transfer to saturated fluids in convective flow.* Industrial & engineering chemistry process design and development, 1966. **5**(3): p. 322-329.

51. Lockhart, R. and R. Martinelli, *Proposed correlation of data for isothermal two-phase, two-component flow in pipes.* Chem. Eng. Prog, 1949. **45**(1): p. 39-48.

52. Rouhani, S.Z. and E. Axelsson, *Calculation of void volume fraction in the subcooled and quality boiling regions.* International Journal of Heat and Mass Transfer, 1970. **13**(2): p. 383-393.

53. Friedel, L. *Improved friction pressure drop correlations for horizontal and vertical two-phase pipe flow*. in *European two-phase group meeting, Ispra, Italy*. 1979.

Appendix A: Air Flow Velocity Profiling Data

The air flow velocity was measured using a probe type hand held anemometer. The coordinate was defined by the tube number and the distance from the inlet side of the heat exchanger, which was illustrated in Figure 49.

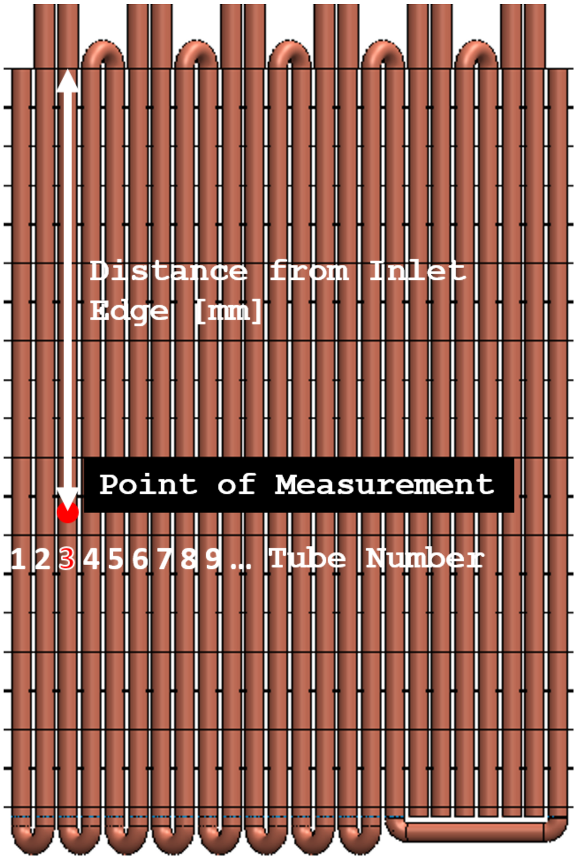

Figure 49 Schematic for the air speed measurement positions.

The air flow velocity distribution is plotted in Figure 50. It is apparent that there was a significant gradient in the air velocity distribution across the tubes as the air velocity almost doubled from the second tube to the sixteenth tube. As the magnitude of air velocity at various position was dependent on the fan speed, the distribution was different for different tests that used different fan speed.

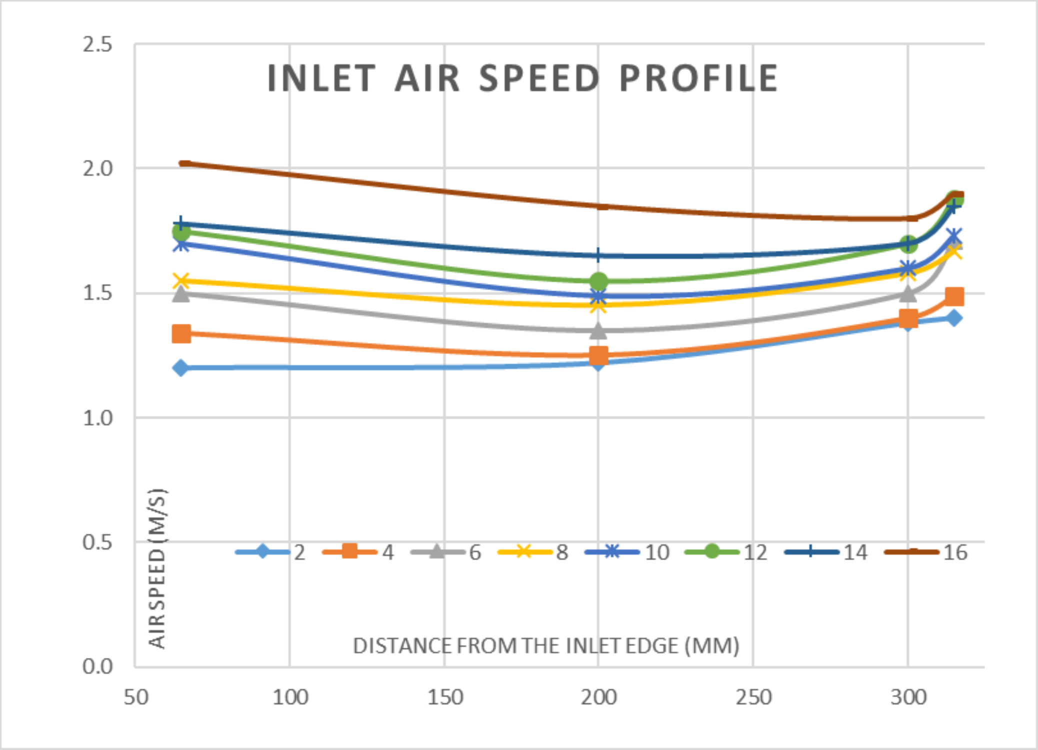

Figure 50 Air speed profile at various locations at the heat exchanger.

Appendix B: Fin Efficiency Calculation

The fin efficiency was calculated based on the rectangular fin model for staggered tube bundle proposed by Hong and Webb [44]:

$$\eta = \frac{tanh(m \cdot r_i \cdot \Phi)}{m \cdot r_i \cdot \Phi} \tag{33}$$

where $\Phi = (\frac{ro}{r_i} - 1) \cdot (1 + 0.35 \cdot ln\left(\frac{ro}{r_i}\right))$

$ro = 1.28 \cdot \varphi \cdot \sqrt{\beta - 0.2} \cdot r_i$

$W = 7.5\, mm$

$L = 12\, mm$

$\varphi = \frac{W}{r_i}$

$\beta = \frac{L}{W}$

$m = \sqrt{2 \cdot \frac{h_a}{k_{fin} \cdot b}}$

$b =$ fin thickness [m]

k_{fin} = thermal conductivity of fin [W/m-K].

The values of parameter *W* and *L* were determined using the cross-sectional schematic of a fin and the holes in it as shown in Figure 51:

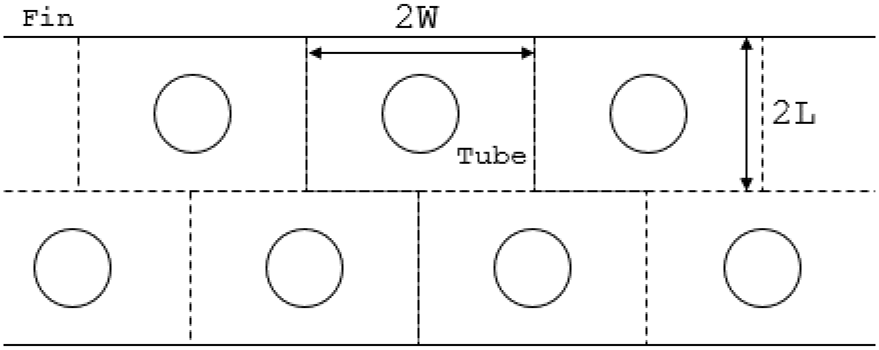

Figure 51 Cross section view of a fin and the holes for tubes. (Dash lines are imaginary)

Appendix C: Air Side Heat Transfer Coefficient Calculation

The heat transfer coefficient at the air side was calculated using the correlation for plain fin-and-tube heat exchangers with staggered tube arrangements proposed by Kim et. al [45] in 1999. From an inspection of the schematic of the heat exchanger used in Kim's tests as shown in Figure 52, it is apparent that the heat exchanger used in current study is highly similar in structure. Thus, it became valid to use Kim's correlation to estimate the air side heat transfer coefficient of the test section used in current study.

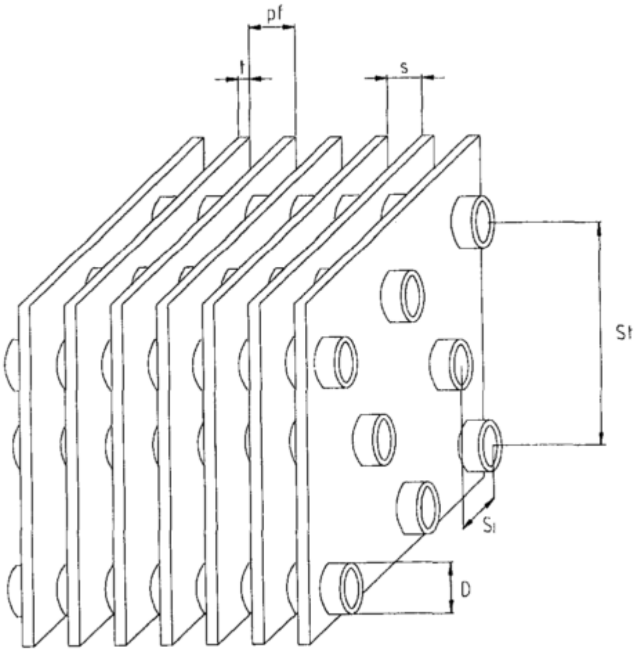

Figure 52 Schematic drawing of the heat exchanger used in Kim's tests. [45]

In general, the heat transfer coefficient of a single-phase flow h_a can be expressed in the following equation:

$$h_a = St \cdot G_a \cdot cp_a \tag{34}$$

where $St = \text{Stanton Number} = j_a \cdot Pr_a^{\frac{2}{3}}$

$j_a =$ Colburn j factor of air flow through the heat exchanger

$G_a =$ mass flux of air flow [kg/m^2-s]

$Pr_a =$ Prandtl number of air

$cp_a =$ specific heat of air [J/kg-K]

Thermal properties of fluids like the specific heat, Prandtl number and viscosity were calculated using a package in Python called CoolProp (coolprop.org). Kim's correlation for the Colburn j factor of air flow through the heat exchanger can be written in the expression below:

$$\begin{aligned} j_a = 0.163 \cdot Re_a^{-0.369} \cdot \left(\frac{s_t}{s_l}\right)^{0.106} \cdot \left(\frac{s}{D_{ha}}\right)^{0.0138} \cdot \left(\frac{s_t}{D_{ha}}\right)^{0.13} \cdot [1.043 \\ \cdot \left(Re_a^{-0.14} \cdot \left(\frac{s_t}{s_l}\right)^{-0.564} \cdot \left(\frac{s}{D_{ha}}\right)^{-0.123} \cdot \left(\frac{s_t}{D_{ha}}\right)^{1.17}\right]^{3-N_r} \end{aligned} \tag{35}$$

where $Re_a = \frac{G_a \cdot D_{ha}}{\mu_a}$ = Reynolds number of the air flow

$D_{ha} =$ hydraulic diameter of the air flow passage = outside tube diameter [m]

$s_t =$ maximum vertical distance between centerline of tubes, where vertical is defined as the direction along the direction of the air flow. [m]

$s_l =$ minimum horizontal distance between centerline of tubes, where horizontal is defined as the direction normal to the direction of the air flow. [m]

$s =$ spacing between adjacent fins [m]

$N_r =$ number of rows of tubes in the vertical direction, where in the current test section, this value is two.

According to Kim [45], this correlation predicts 90 percent of the data within ±20 percent for heat exchangers with two rows. The root mean squire error is 12.6 percent.